Transport in Porous Media manuscript No.
(will be inserted by the editor)

A Compressible Fluid Flow Model Coupling Channel and Porous Media Flows and Its Application to Fuel Cell Materials

Alex Jarauta[1] · **Valentin Zingan**[1] · **Peter Minev**[2] · **Marc Secanell**[1]

Received: date / Accepted: date

Abstract A multi-dimensional, compressible fluid flow solver, valid in both channel and porous media, is derived by volume-averaging the Navier-Stokes equations. By selecting an appropriate average density/velocity pair, a continuous, stable solution is obtained for both pressure and velocity. The proposed model is validated by studying the pressure drop of two commonly used experimental setups to measure in-plane and through-plane permeability of fuel cell porous media. Numerical results show that the developed model is able to reproduce the experimentally measured pressure drop at varying flow rates. Further, it highlights that previously used methods of extracting permeability, which rely on the use of simplified one-dimensional models, are not appropriate when high flow rates are used to study the porous media. At high flow rates, channel-porous media interactions cannot be neglected and can result in incorrect permeability estimations. For example, at flow rates of 1 SLPM a discrepancy of 12% in pressure drop was observed when using previous permeability values instead of the values obtained in the article using the proposed 3D model. Given that at high flow rate one-dimensional models might not be appropriate, previous estimations of Forchheimer permeability might not be accurate. To illustrate the suitability of the numerical model to fuel cell applications, fluid flow by-pass in serpentine and interdigitated fuel cell flow channels is also investigated.

Keywords Polymer electrolyte fuel cell · Flow in porous media · Method of volume averaging · Compressible Navier-Stokes equations · Brinkman equation · Darcy-Forchheimer equation · coupling free and porous medium flows

[1] Energy Systems Design Lab (ESDLab)
University of Alberta, Edmonton, Canada

[2] Department of Mathematical and Statistical Sciences
University of Alberta, Edmonton, Canada

M. Secanell, corresponding author
E-mail: secanell@ualberta.ca

1 Introduction

Analysis of fluid flows in porous media is required in many engineering applications such as fuel cells, enhanced oil recovery, chemical reactors, and environmental problems. Mass, momentum, and energy transport in porous media are governed by its internal porous structure. Despite the significant growth in computational resources, the computational effort required to model transport phenomena in such complex geometries is still beyond their capacity. Therefore, macroscopic porous medium approximations, based on averaging the pore-scale over a representative elementary volume, are still commonly used (Whitaker (1999); Gray and Lee (1977); Whitaker (1969); Hendrick et al. (2012)).

The first macroscopic empirical model for one-dimensional incompressible flows through porous media was proposed by Darcy (1857). Darcy equation provides the simplest linear relationship between fluid flow parameters in porous media under the physically reasonable assumption that fluid flows are very slow. A nonlinear correction to Darcy equation for higher pore-scale flow velocity was proposed by Forchheimer (1901).

Many practical engineering applications, as for example polymer electrolyte fuel cells, deal with the systems composed of free flows in channels coupled with flows in porous media. Since both Darcy equation and Forchheimer-extended Darcy flow model do not contain a shear-stress term (i.e., $\mu\nabla^2\boldsymbol{v}$ term), they cannot be used at the interface between channels and porous media because they do not accept the use of no-slip or partial-slip boundary conditions at the interface between impermeable walls and porous media (Beavers and Joseph (1967)). Starting from the original experimental work of Beavers and Joseph (1967), the coupling of free channel flows governed by incompressible Stokes/Navier-Stokes equations with porous medium flows governed by either Darcy equation or Darcy-Forchheimer equation has been extensively studied in the literature. The key idea of these coupling techniques assumes imposing some sort of special boundary conditions on the channel-porous medium interface. Examples of such interface conditions are Levy and Sanchez-Palencia (1975), Beavers and Joseph (1967), and Saffman (1971).

Most of the finite element formulations developed for the coupled problem are based on appropriate combinations of stable elements in both flow regions. Very often the Navier-Stokes equations in the fluid domain are discretized by Taylor-Hood elements and the Darcy equations in the porous medium are discretized by Raviart-Thomas elements. Alternatively, mortar finite element techniques, discontinuous Galerkin schemes, and stabilized formulations have also been applied to solve the coupled problems. The coupled Stokes and Darcy models have been studied for example in Burman and Hansbo (2007); Bernardi et al. (2008); Urquiza et al. (2008). The Navier-Stokes and Darcy coupling has been analyzed by Discacciati and Quarteroni (2009); Badea et al. (2010); Chidyagwai and Rivière (2009). Since the velocity in the Darcy equations is curl-free while in the Stokes/Navier-Stokes equations it is not, their coupling at the common interface is not very natural and therefore non-trivial. It brings additional problems at the lines of intersection of impermeable walls and the interface between the fluid and porous domains. Indeed, from the porous side, only the normal component of the velocity can be prescribed while from the fluid side, both components are to be prescribed. Additionally, the use of different types of discretization in the two different areas,

and the special care needed to couple them, complicates the implementation of such algorithms.

If the porosity of the porous media is high, as for example in fibrous materials and foams (Auriault (2009)), an alternative to the Darcy equation is given by the Brinkman equation. The Brinkman equation can be naturally coupled with incompressible Stokes/Navier-Stokes flows in the fluid domain and can be supplemented with appropriate boundary conditions at the impermeable walls of the porous domain. Since the porosity of the gas diffusion layer of polymer electrolyte fuel cell is relatively high, the Brinkman model is widely used to model it. In order to account for inertial effects and non-linear drag in the porous medium, the steady-state Brinkman momentum equation is often corrected by adding a convective term and a Forchheimer drag force term (see for example Hsu and Cheng (1990); Vafai and Tien (1981)).

Srinivasan and Rajagopal (2014) and Rajagopal (2007), starting from the compressible Navier-Stokes equations, and invoking more and more severe restrictions, obtained first the Brinkman, and then the Darcy models of flows in porous media. Many articles have used the Brinkman equations to model the coupled flow in the gas channel and the gas diffusion porous layer in polymer electrolyte fuel cells. The effect of porous matrix permeability on convective transport in a gas diffusion layer (GDL) was studied by Pharoah (2005); Saha and Oshima (2012), and Park and Li (2007). The pressure drop along with cross flow behaviour in polymer electrolyte fuel cells with serpentine gas channels was investigated by Saha et al. (2008); Park and Li (2011); Salahuddin et al. (2013), and Zhang et al. (2019b). The system composed of serpentine gas channels with a trapezoidal cross-sectional shape and underlying GDL was studied by Sun et al. (2006). Numerical investigation of the cross flow effects on the performance of polymer electrolyte fuel cells was carried out by Salahuddin and Oshima (2013); Hashemi et al. (2012); Nguyen et al. (2004). In most of these studies, an incompressible form of the Navier-Stokes/Brinkman equations was used. Only a few of these studies considered the compressible form of the momentum equation (Nguyen et al. (2004); Hashemi et al. (2012); Salahuddin and Oshima (2013); Zhang et al. (2019b)). The permeability coefficients were either estimated from empirical correlations (Gebart (1992)) or obtained from literature data based on a simplified model (Gostick et al. (2006); Pant et al. (2012); Carrigy et al. (2013); Mangal et al. (2015)).

The use of an incompressible form of the Navier-Stokes/Brinkman equation in fuel cells is puzzling since the changing composition of the reacting gas mixture can lead to large changes in the mixture density as it flows through the channels and the porous media, especially in the anode channel. Santamaria et al. emphasized the importance of using a compressible fluid flow model for flow-field designs that force the gas flow through the porous material, such as interdigitated channels (Santamaria et al. (2013)), and many other studies in the literature have also considered a compressible fluid flow model when analyzing fuel cells with interdigitated channels (e.g., Yu et al. (2009); Jian et al. (2014); Mahmoudi et al. (2016); Li and Sundén (2018)). A compressible form of the Navier-Stokes/Brinkman equation appears therefore to be more appropriate. Using the compressible Navier-Stokes/Brinkman equation in channels and porous media might however lead to unstable numerical schemes depending on the volume-averaging technique used to define the density and velocity in the porous media. Therefore, an objective of this paper is to develop a numerically stable volume-averaged discrete model

based on the steady-state, compressible Navier-Stokes equations, and use it to study gas flows in a channel interfaced with a porous layer. In the process, a clear interpretation of the solution variables will be provided.

Experimental methods for measuring permeability usually involve the use of a one-dimensional porous media model developed using either Darcy or Darcy-Forchheimer equation. The permeability coefficient is estimated by fitting the experimentally measured pressure drop across the porous media at different mass flow rates to the one-dimensional model predictions. A compressible form of the fluid flow equations is usually used to estimate the permeability tensor $\hat{\boldsymbol{K}}$ and nonlinear Forchheimer correction tensor $\hat{\boldsymbol{\beta}}$, e.g., Feser et al. (2006); Gostick et al. (2006); Gurau et al. (2007); Ismail et al. (2009); Pant et al. (2012); Carrigy et al. (2013). Under the conditions typically used in experiments, the incompressible assumption has been shown to underestimate the through-plane and in-plane permeability components by 9% (Ismail et al. (2009)) and 23% (Ismail et al. (2010)), respectively. Using a one-dimensional model to estimate the permeability also presumes that multi-dimensional effects such as fluid flow patterns in the channel and channel/porous media interactions are negligible. Given the assumptions used to obtain the permeability coefficients, its appropriateness for use in multi-dimensional fuel cell models requires further studies. Furthermore, it appears that a more appropriate methodology to obtain the permeability coefficient would be to use the same multi-dimensional model that would then be used in a fuel cell simulation.

In this article, a multi-dimensional, compressible fluid flow solver based on the Navier-Stokes equations is derived using the volume-average method proposed by Whitaker (Whitaker (1999)). The fluid flow solver, valid in both channel and porous media, is used to estimate the most appropriate density/velocity pair for averaging, and then to simulate the fluid flow in a through-plane and in-plane experimental permeability setup. The latter results allow us to analyze the validity of the previous one-dimensional models used to extract the permeability tensor, and to obtain a more accurate estimation of the tensor. The numerical model and newly estimated permeability coefficients are finally used to study fluid flow by-pass in serpentine and interdigitated channels.

To the authors' knowledge, this is the first attempt in the literature to evaluate four pairs of volume-averaged variables and discuss a) the volume-averaged solution variable pairs that result in discontinuities between the porous media and the channel and their numerical stability; b) the relationship between volume-averaged solution variables and permeability, and their impact on pressure drop predictions; and, c) the appearance of three-dimensional channel-porous media interactions in experimental setups used to measure permeability, which can result in incorrect permeability estimates at high velocity.

2 Mathematical Model

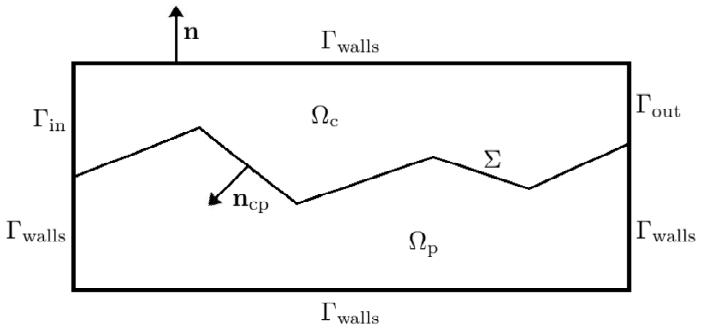

Fig. 1 An example of the computational domain.

2.1 Preliminaries

Let $\Omega \subset \mathbb{R}^d$, $d = 2, 3$, be an open connected domain with boundary Γ. The domain Ω is split into two parts: channels (Ω_c) and porous media (Ω_p). The boundary Γ consists of three parts: the inflow boundary Γ_in, the outflow boundary Γ_out, and solid impermeable walls Γ_walls such that $\Gamma = \Gamma_\mathrm{in} \cup \Gamma_\mathrm{out} \cup \Gamma_\mathrm{walls}$. The interface between channels and porous media is denoted by Σ. The outer normal vector on Γ is denoted by $\boldsymbol{n}$ and a pair of tangential vectors by $\{\boldsymbol{\tau}_\alpha\}_{\alpha=1}^{d-1}$. The tangential vectors are chosen such that the set $(\boldsymbol{n}, \boldsymbol{\tau}_1, ..., \boldsymbol{\tau}_{d-1})$ builds an orthonormal basis in d-dimensional space. The normal vector on Σ directed from channels to porous media is denoted by $\boldsymbol{n}_\mathrm{cp}$. An example of the computational domain is shown in Figure 1.

2.2 Governing Equations in the Channels

In order to model the fluid flow in the channels, the steady-state compressible, isothermal, and barotropic Navier-Stokes equations are used. The equations read as

$$\nabla \cdot (\rho \boldsymbol{v}) = 0 \qquad \text{in} \quad \Omega_\mathrm{c}, \tag{1}$$

$$\nabla \cdot (\rho \boldsymbol{v} \otimes \boldsymbol{v}) = \nabla \cdot \left(-p\hat{\boldsymbol{I}} + \hat{\boldsymbol{\sigma}}\right) + \rho \boldsymbol{g} \qquad \text{in} \quad \Omega_\mathrm{c}, \tag{2}$$

$$p = \rho R T, \tag{3}$$

$$\hat{\boldsymbol{\sigma}} = 2\mu \nabla_s \boldsymbol{v} + \lambda \left(\nabla \cdot \boldsymbol{v}\right) \hat{\boldsymbol{I}}, \tag{4}$$

$$\lambda = -\frac{2}{3}\mu, \tag{5}$$

where ρ is the fluid density, $\boldsymbol{v}$ is the fluid velocity, p is the fluid pressure, $\hat{\boldsymbol{\sigma}}$ is the fluid Newtonian shear stress tensor, $\boldsymbol{g}$ is the gravity acceleration, R is the specific gas constant, T is the fluid constant temperature, μ and λ are the fluid constant dynamic and bulk viscosities respectively, $\hat{\boldsymbol{I}}$ is the identity tensor, and $\nabla_s = \frac{1}{2}\left(\nabla + \nabla^\mathrm{T}\right)$ is the symmetric gradient.

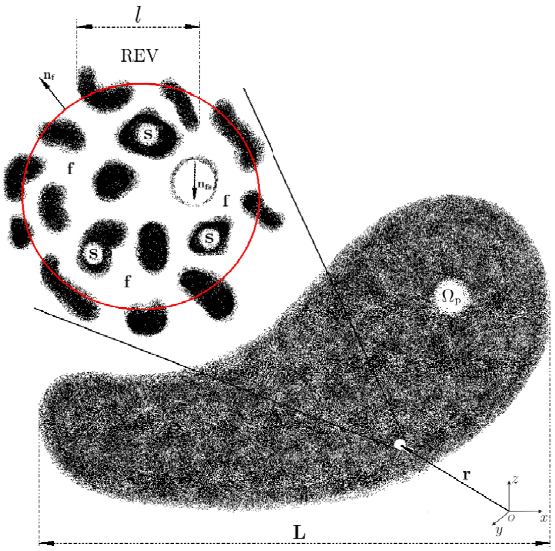

Fig. 2 Representative Elementary Volume

2.3 Governing Equations in Porous Media

2.3.1 Method of volume averaging

It is a challenging problem to determine all details of fluid flows inside a network of pores and some type of averaging procedure is commonly used to develop the governing equations of the fluid inside the porous media. The method of volume averaging (Whitaker (1999)) is based on the assumption that locally averaged properties will suffice for design purposes. The method proceeds by associating each point $\boldsymbol{r}$ in a porous domain Ω_{p} (see Figure 2) with a small volume, called a representative elementary volume (REV). The size of the REV is chosen such that $l \ll \mathrm{diam\,(REV)} \ll L$, where l and L are the characteristic micro- and macro- sizes of the porous region respectively. The volumes occupied by fluid and solid phases within the REV are denoted by $V_{\mathrm{f}}(\boldsymbol{r})$ and $V_{\mathrm{s}}(\boldsymbol{r})$ respectively with $V_{\mathrm{REV}} = V_{\mathrm{f}}(\boldsymbol{r}) + V_{\mathrm{s}}(\boldsymbol{r})$, where V_{REV} is the total volume of the REV. The total area of the interface between the fluid phase within the REV and the fluid phase surrounding the REV is denoted by $A_{\mathrm{f}}(\boldsymbol{r})$. The total area of the interface between the fluid and solid phases that is within the REV is denoted by $A_{\mathrm{fs}}(\boldsymbol{r})$.

2.3.2 Local averaging procedure

Generally, two averages of a function ϕ are used in the method of volume averaging, the phase average and the intrinsic phase average. The phase average is defined as (Whitaker (1999))

$$<\phi>= \frac{1}{V_{\mathrm{REV}}} \int_{V_{\mathrm{f}}(\boldsymbol{r})} \phi \; dV. \tag{6}$$

The intrinsic phase average is defined as (Whitaker (1999))

$$<\phi>^{\mathrm{f}} = \frac{1}{V_{\mathrm{f}}(\boldsymbol{r})} \int_{V_{\mathrm{f}}(\boldsymbol{r})} \phi \; dV. \tag{7}$$

The obvious relationship between these two averages is

$$<\phi> = \epsilon \; <\phi>^{\mathrm{f}}, \tag{8}$$

where $\epsilon = \frac{V_{\mathrm{f}}(\boldsymbol{r})}{V_{\mathrm{REV}}}$ is the porosity of the REV. Using definitions (6) and (7) the following relations can be shown

$$<A\phi + B\psi> = A \; <\phi> + B \; <\psi>, \tag{9}$$

$$<A\phi + B\psi>^{\mathrm{f}} = A \; <\phi>^{\mathrm{f}} + B \; <\psi>^{\mathrm{f}}, \tag{10}$$

where A and B are arbitrary constants and ψ is a function. If $\delta\phi$ is a deviation of ϕ from the expected mean value $<\phi>^{\mathrm{f}}$ such that $\forall \boldsymbol{\xi} \in V_{\mathrm{f}}(\boldsymbol{r}) : \phi = <\phi>^{\mathrm{f}} + \delta\phi$ and $<\delta\phi> = <\delta\phi>^{\mathrm{f}} = 0$, then it can also be shown that

$$<\phi\psi> = \frac{1}{\epsilon} \; <\phi><\psi> + <\delta\phi\delta\psi>, \tag{11}$$

$$<\phi\psi>^{\mathrm{f}} = <\phi>^{\mathrm{f}}<\psi>^{\mathrm{f}} + <\delta\phi\delta\psi>^{\mathrm{f}}. \tag{12}$$

If the size of the REV satisfies the condition diam (REV) $\gg l$, then the averages of products of deviations $\delta\phi$ and $\delta\psi$ in the right hand side of equations (11) and (12) can be neglected and the equations themselves reduce to

$$<\phi\psi> \approx \frac{1}{\epsilon} \; <\phi><\psi>, \tag{13}$$

$$<\phi\psi>^{\mathrm{f}} \approx <\phi>^{\mathrm{f}}<\psi>^{\mathrm{f}}. \tag{14}$$

2.3.3 Spatial averaging theorem

The connection between the equations governing single phase transport phenomena in pores, i.e., equations (1)-(5), and those averaged over the REV is established by means of the spatial averaging theorem (Gray and Lee (1977); Whitaker (1969); Howes and Whitaker (1985)). Let $<\nabla\phi>$ be a phase average of the gradient of some continuous function ϕ. The spatial averaging theorem can be obtained by using the divergence theorem. The divergence theorem applied to the $<\nabla\phi>$ yields

$$\frac{1}{V_{\mathrm{REV}}} \int_{V_{\mathrm{f}}(\boldsymbol{r})} \nabla\phi \; dV = \frac{1}{V_{\mathrm{REV}}} \int_{A_{\mathrm{f}}(\boldsymbol{r})} \phi \boldsymbol{n}_{\mathrm{f}} \; dA + \frac{1}{V_{\mathrm{REV}}} \int_{A_{\mathrm{fs}}(\boldsymbol{r})} \phi \boldsymbol{n}_{\mathrm{fs}} \; dA. \tag{15}$$

where $\boldsymbol{n}_{\mathrm{f}}$ denotes the unit normal vector outwardly directed from fluid to fluid phase, and $\boldsymbol{n}_{\mathrm{fs}}$ is the unit normal vector directed from fluid to solid phase within the REV. Then it can be shown that (Howes and Whitaker (1985))

$$\frac{1}{V_{\mathrm{REV}}} \int_{A_{\mathrm{f}}(\boldsymbol{r})} \phi \boldsymbol{n}_{\mathrm{f}} \; dA = \frac{1}{V_{\mathrm{REV}}} \nabla \int_{V_{\mathrm{f}}(\boldsymbol{r})} \phi \; dV \tag{16}$$

and finally

$$\frac{1}{V_{\mathrm{REV}}} \int_{V_{\mathrm{f}}(\boldsymbol{r})} \nabla\phi \; dV = \frac{1}{V_{\mathrm{REV}}} \nabla \int_{V_{\mathrm{f}}(\boldsymbol{r})} \phi \; dV + \frac{1}{V_{\mathrm{REV}}} \int_{A_{\mathrm{fs}}(\boldsymbol{r})} \phi \boldsymbol{n}_{\mathrm{fs}} \; dA \tag{17}$$

or

$$<\nabla\phi>=\nabla<\phi>+\frac{1}{V_{\mathrm{REV}}}\int_{A_{\mathrm{fs}}(\boldsymbol{r})}\phi\boldsymbol{n}_{\mathrm{fs}}\,dA. \tag{18}$$

It is easy to show that the following extensions of equation (18) are also valid (Whitaker (1999))

$$<\nabla\boldsymbol{a}>=\nabla<\boldsymbol{a}>+\frac{1}{V_{\mathrm{REV}}}\int_{A_{\mathrm{fs}}(\boldsymbol{r})}\boldsymbol{a}\otimes\boldsymbol{n}_{\mathrm{fs}}\,dA, \tag{19}$$

$$<\nabla\cdot\boldsymbol{a}>=\nabla\cdot<\boldsymbol{a}>+\frac{1}{V_{\mathrm{REV}}}\int_{A_{\mathrm{fs}}(\boldsymbol{r})}\boldsymbol{a}\cdot\boldsymbol{n}_{\mathrm{fs}}\,dA, \tag{20}$$

$$<\nabla\cdot\hat{\boldsymbol{T}}>=\nabla\cdot<\hat{\boldsymbol{T}}>+\frac{1}{V_{\mathrm{REV}}}\int_{A_{\mathrm{fs}}(\boldsymbol{r})}\hat{\boldsymbol{T}}\boldsymbol{n}_{\mathrm{fs}}\,dA, \tag{21}$$

where $\boldsymbol{a}$ and $\hat{\boldsymbol{T}}$ are some continuous vectorial and tensorial fields respectively. It should be noted that the nabla operator in $\nabla\phi$ and $\nabla<\phi>$ has different meanings and length scales. While in the former case ∇ is applied to the fluid phase within the REV and scaled as $\frac{1}{l}$, in the latter case ∇ relates to the sequence of control volumes continuously occupying the space of porous domain Ω_{p} and therefore it is scaled as $\frac{1}{L}$.

2.3.4 Volume-averaged governing equations

In this section, the pore-scale point-wise governing equations (1)-(5) are averaged over the REV located in the neighbourhood of a spatial point $\boldsymbol{r}$. We start with the mass conservation equation (1). Since $\nabla\cdot(\rho\boldsymbol{v})=0$ in $V_{\mathrm{f}}(\boldsymbol{r})$, it follows that $<\nabla\cdot(\rho\boldsymbol{v})>=0$, and an application of the spatial averaging theorem (20) leads to the following equality

$$\nabla\cdot<\rho\boldsymbol{v}>+\frac{1}{V_{\mathrm{REV}}}\int_{A_{\mathrm{fs}}(\boldsymbol{r})}\rho\boldsymbol{v}\cdot\boldsymbol{n}_{\mathrm{fs}}\,dA=0. \tag{22}$$

The surface integral in this expression is equal to zero because of the orthogonality of vectors $\boldsymbol{v}$ and $\boldsymbol{n}_{\mathrm{fs}}$. Taking into account equation (13), the following form of the volume-averaged mass conservation equation is obtained:

$$\nabla\cdot\left(\frac{1}{\epsilon}<\rho><\boldsymbol{v}>\right)=0, \tag{23}$$

where $<\rho>$ and $<\boldsymbol{v}>$ are the phase averages according to equation (6).

The same procedure is applied to the momentum conservation equation (2) to obtain the following volume-averaged equation:

$$\begin{aligned}&\nabla\cdot\left(\frac{1}{\epsilon^2}<\rho><\boldsymbol{v}>\otimes<\boldsymbol{v}>\right)+\frac{1}{V_{\mathrm{REV}}}\int_{A_{\mathrm{fs}}(\boldsymbol{r})}(\rho\boldsymbol{v}\otimes\boldsymbol{v})\,\boldsymbol{n}_{\mathrm{fs}}\,dA=\\&\nabla\cdot\left(-<p>\hat{\boldsymbol{I}}+<\hat{\boldsymbol{\sigma}}>\right)+\frac{1}{V_{\mathrm{REV}}}\int_{A_{\mathrm{fs}}(\boldsymbol{r})}\left(-p\hat{\boldsymbol{I}}+\hat{\boldsymbol{\sigma}}\right)\boldsymbol{n}_{\mathrm{fs}}\,dA+<\rho>\boldsymbol{g}\end{aligned} \tag{24}$$

with

$$<p>=<\rho>RT \tag{25}$$

and

$$<\hat{\boldsymbol{\sigma}}>= 2\mu \left(\nabla_s <\boldsymbol{v}> + \frac{1}{V_{\text{REV}}} \int_{A_{\text{fs}}(\boldsymbol{r})} (\boldsymbol{v} \otimes \boldsymbol{n}_{\text{fs}})_s \; dA \right) + \lambda_{\text{eff}} \Big(\nabla \cdot <\boldsymbol{v}> \Big) \hat{\boldsymbol{I}}. \tag{26}$$

The boundary integral in the left hand side of the equation (24) is identically equal to zero because of the orthogonality of vectors $\boldsymbol{v}$ and $\boldsymbol{n}_{\text{fs}}$, i.e.,

$$(\rho \boldsymbol{v} \otimes \boldsymbol{v})\, \boldsymbol{n}_{\text{fs}} \Big|_{A_{\text{fs}}(\boldsymbol{r})} = \rho v_i \sum_j v_j n_{\text{fs},j} \Big|_{A_{\text{fs}}(\boldsymbol{r})} = \boldsymbol{0} \tag{27}$$

It is then assumed that no-slip boundary conditions are applied at the fluid-solid interface within the REV such that the integral over $A_{\text{fs}}(\boldsymbol{r})$ in equation (26) vanishes. The last integral term in equation (24) contains the information on how the microstructure of the porous matrix affects the fluid flow through exerting pressure and friction forces. Its estimation entirely depends on the local geometry and flow regime. Several attempts have been made to constitutively correlate this integral term with the macroscopic volume-averaged velocity and microstructure properties for incompressible flows (Hsu and Cheng (1990); Liu and Masliyah (1996); Whitaker (1996); Rajagopal (2007)). Whitaker (1999) approximated this term with Darcy's law. In the fuel cell context, however, the extended Darcy-Forchheimer law should be considered to account for inertial effects in the porous layers. Thus, in the present paper the following closure relation is used:

$$\frac{1}{V_{\text{REV}}} \int_{A_{\text{fs}}(\boldsymbol{r})} \Big(-p\hat{\boldsymbol{I}} + \hat{\boldsymbol{\sigma}} \Big)\, \boldsymbol{n}_{\text{fs}} \; dA \approx -\mu \hat{\boldsymbol{K}}^{-1} <\boldsymbol{v}> - \hat{\boldsymbol{\beta}} <\rho> \mid <\boldsymbol{v}> \mid <\boldsymbol{v}>, \tag{28}$$

where $\hat{\boldsymbol{K}}$ is the porous matrix permeability and $\hat{\boldsymbol{\beta}}$ is frequently referred to as the Forchheimer permeability and relates to the nonlinear correction allowing for higher pore-scale fluid velocity.

Equations (23) and (24) are obtained in terms of both phase-averaged density $<\rho>$ and velocity $<\boldsymbol{v}>$. As discussed below, it is more appropriate to use an intrinsic phase-averaged velocity $<\boldsymbol{v}>^{\text{f}}$ such that the volume-averaged steady-state compressible and isothermal Navier-Stokes equations become

$$\nabla \cdot \Big(<\rho><\boldsymbol{v}>^{\text{f}} \Big) = 0 \quad \text{in} \quad \Omega_{\text{p}}, \tag{29}$$

$$\nabla \cdot \Big(<\rho><\boldsymbol{v}>^{\text{f}} \otimes <\boldsymbol{v}>^{\text{f}} \Big) = \nabla \cdot \Big(- <p>\, \hat{\boldsymbol{I}} + <\hat{\boldsymbol{\sigma}}>^{\text{f}} \Big) - \mu \hat{\boldsymbol{K}}^{-1} \epsilon <\boldsymbol{v}>^{\text{f}} - \hat{\boldsymbol{\beta}} <\rho> |\epsilon <\boldsymbol{v}>^{\text{f}}| \epsilon <\boldsymbol{v}>^{\text{f}} + <\rho>\, \boldsymbol{g} \quad \text{in} \quad \Omega_{\text{p}}, \tag{30}$$

$$<p> = <\rho>\, RT, \tag{31}$$

$$<\hat{\boldsymbol{\sigma}}>^{\text{f}} = 2\mu \nabla_s \epsilon <\boldsymbol{v}>^{\text{f}} + \lambda \Big(\nabla \cdot \epsilon <\boldsymbol{v}>^{\text{f}} \Big) \hat{\boldsymbol{I}}, \tag{32}$$

$$\lambda = -\frac{2}{3}\mu. \tag{33}$$

2.4 Boundary Conditions at the Interface Between Channels and Porous Media

Both systems of equations governing the fluid flow in the channels (1)-(5) and the porous media (29)-(33) are coupled to each other through boundary conditions

imposed on the interface between channels and porous media, i.e., the interface Σ. Generally, there are four different combinations of solution variables that one can use in the structure of volume-averaged equations (29)-(33) governing fluid flow in porous media. The physics of the problem clearly requires the continuity of mass, momentum, and diffusive fluxes across this interface, i.e.:

$$\rho \boldsymbol{v} \cdot \boldsymbol{n}_{\mathrm{cp}}\Big|_{\Sigma} = <\rho><\boldsymbol{v}>^{\mathrm{f}} \cdot \boldsymbol{n}_{\mathrm{cp}}\Big|_{\Sigma}, \tag{34}$$

$$(\rho \boldsymbol{v} \otimes \boldsymbol{v})\, \boldsymbol{n}_{\mathrm{cp}}\Big|_{\Sigma} = \left(<\rho><\boldsymbol{v}>^{\mathrm{f}} \otimes <\boldsymbol{v}>^{\mathrm{f}}\right) \boldsymbol{n}_{\mathrm{cp}}\Big|_{\Sigma}, \tag{35}$$

$$\left(-p\hat{\boldsymbol{I}} + \hat{\boldsymbol{\sigma}}\right) \boldsymbol{n}_{\mathrm{cp}}\Big|_{\Sigma} = \left(- <p>\, \hat{\boldsymbol{I}} + <\hat{\boldsymbol{\sigma}}>^{\mathrm{f}}\right) \boldsymbol{n}_{\mathrm{cp}}\Big|_{\Sigma}. \tag{36}$$

Solving equations (34) and (35) with respect to densities ρ and $<\rho>$ and normal velocity components v_n and $<v_n>^{\mathrm{f}}$ yields the following boundary conditions at the interface Σ

$$<\rho>\Big|_{\Sigma} = \rho\Big|_{\Sigma}, \tag{37}$$

$$<v_n>^{\mathrm{f}}\Big|_{\Sigma} = v_n\Big|_{\Sigma}. \tag{38}$$

As it can be seen from equations (37) and (38), both density and velocity fields are continuous across the interface Σ. Some combinations of density and velocity however yield non-zero jump boundary conditions at the interface between channels and porous media. For example, using a pair $(<\rho>, <\boldsymbol{v}>)$ leads to a discontinuity in the velocity field. The information on different sets of solution variables along with associated jump boundary conditions at the interface Σ is reported in Table 1. It should be noted that only the set of solution variables $\left(<\rho>, <\boldsymbol{v}>^{\mathrm{f}}\right)$ provides no jumps in both density and velocity fields across the interface Σ, and therefore it is used in the spatially averaged equations (29)-(33).

2.5 Single Domain Approach and Boundary Conditions

The two systems of equations (1)-(5) and (29)-(33), abusing notations somewhat, can be written as a single system of governing equations, valid in both subdomains

Table 1 Solution variables in porous media and associated jump boundary conditions at the interface Σ.

Solution variables	Jump boundary conditions
$<\rho>$ and $<\boldsymbol{v}>$	$<\rho>\big\vert_{\Sigma} = \rho\big\vert_{\Sigma}$ $<v_n>\big\vert_{\Sigma} = \varepsilon v_n\big\vert_{\Sigma}$
$<\rho>$ and $<\boldsymbol{v}>^{\mathrm{f}}$	$<\rho>\big\vert_{\Sigma} = \rho\big\vert_{\Sigma}$ $<v_n>^{\mathrm{f}}\big\vert_{\Sigma} = v_n\big\vert_{\Sigma}$
$<\rho>^{\mathrm{f}}$ and $<\boldsymbol{v}>$	$<\rho>^{\mathrm{f}}\big\vert_{\Sigma} = \frac{\rho}{\varepsilon}\big\vert_{\Sigma}$ $<v_n>\big\vert_{\Sigma} = \varepsilon v_n\big\vert_{\Sigma}$
$<\rho>^{\mathrm{f}}$ and $<\boldsymbol{v}>^{\mathrm{f}}$	$<\rho>^{\mathrm{f}}\big\vert_{\Sigma} = \frac{\rho}{\varepsilon}\big\vert_{\Sigma}$ $<v_n>^{\mathrm{f}}\big\vert_{\Sigma} = v_n\big\vert_{\Sigma}$

Ω_{c} and Ω_{p} of the domain Ω, as follows:

$$\nabla \cdot (\rho \boldsymbol{v}) = 0 \quad \text{in} \quad \Omega, \tag{39}$$

$$\nabla \cdot (\rho \boldsymbol{v} \otimes \boldsymbol{v}) = \nabla \cdot \left(-p\hat{\boldsymbol{I}} + \hat{\boldsymbol{\sigma}}\right) + \boldsymbol{F} + \rho \boldsymbol{g} \quad \text{in} \quad \Omega, \tag{40}$$

$$p = \rho R T, \tag{41}$$

$$\hat{\boldsymbol{\sigma}} = 2\mu \nabla_s \boldsymbol{v} + \lambda \left(\nabla \cdot \boldsymbol{v}\right) \hat{\boldsymbol{I}}, \tag{42}$$

$$\lambda = -\frac{2}{3}\mu, \tag{43}$$

$$\boldsymbol{F} = \begin{cases} \boldsymbol{0} & \text{in} \quad \Omega_{\mathrm{c}} \\ -\mu \hat{\boldsymbol{K}}^{-1} \epsilon \boldsymbol{v} - \hat{\boldsymbol{\beta}} \rho \big\vert \epsilon \boldsymbol{v} \big\vert \epsilon \boldsymbol{v} & \text{in} \quad \Omega_{\mathrm{p}} \end{cases}, \tag{44}$$

$$\rho := \begin{cases} \rho & \text{in} \quad \Omega_{\mathrm{c}} \\ <\rho> & \text{in} \quad \Omega_{\mathrm{p}} \end{cases}, \tag{45}$$

$$\boldsymbol{v} := \begin{cases} \boldsymbol{v} & \text{in} \quad \Omega_{\mathrm{c}} \\ <\boldsymbol{v}>^{\mathrm{f}} & \text{in} \quad \Omega_{\mathrm{p}} \end{cases}, \tag{46}$$

where density ρ and velocity $\boldsymbol{v}$ fields have point-wise values in channels and REV-wise values in porous media and $\boldsymbol{F}$ is the Darcy-Forchheimer drag force. To be well-posed, equations (39)-(46) are supplemented with appropriate boundary conditions

at Γ_{in}, Γ_{out}, and Γ_{walls} boundaries defined as

$$\boldsymbol{v}\Big|_{\Gamma_{\text{in}}} = \boldsymbol{v}_{\text{in}}, \qquad \rho\Big|_{\Gamma_{\text{out}}} = \rho_{\text{out}}, \qquad \boldsymbol{v}\Big|_{\Gamma_{\text{walls}}} = \boldsymbol{0} \tag{47}$$

as well as the internal boundary conditions (34)-(36) at the interface between channels and porous media. In addition, a vanishing normal component of the shear stress $\hat{\boldsymbol{\sigma}}$ is assumed at Γ_{out}, that is

$$\hat{\boldsymbol{\sigma}}\boldsymbol{n}\Big|_{\Gamma_{\text{out}}} = \boldsymbol{0}. \tag{48}$$

Alternatively, another set of boundary conditions at the outer boundary Γ can also be used

$$\rho\Big|_{\Gamma_{\text{in}}} = \rho_{\text{in}}, \qquad \rho\Big|_{\Gamma_{\text{out}}} = \rho_{\text{out}}, \qquad \boldsymbol{v}\Big|_{\Gamma_{\text{walls}}} = \boldsymbol{0}, \qquad \hat{\boldsymbol{\sigma}}\boldsymbol{n}\Big|_{\Gamma_{\text{in}}} = \hat{\boldsymbol{\sigma}}\boldsymbol{n}\Big|_{\Gamma_{\text{out}}} = \boldsymbol{0}. \tag{49}$$

3 Numerical Procedure

3.1 Finite Element Approximation

The domain Ω is discretized into the set $\mathbb{T}_h$ of non-overlapping finite elements K such that $\bigcup_{K\in\mathbb{T}_h} \bar{K} = \bar{\Omega}$. The elements are assumed to be either quadrilaterals in two space dimensions or hexahedra in three space dimensions. Choosing a proper pair of discretization spaces $\mathcal{M}_h^d$ and $\mathcal{V}_h$ for the velocity and density, the following standard discrete Galerkin formulation is obtained:

Find a $(\rho_h, \boldsymbol{v}_h) \in \mathcal{V}_h \times \mathcal{M}_h^d$ such that

$$\forall q_h \in \mathcal{V}_h :$$

$$-\int_\Omega \nabla q_h \cdot \rho_h \boldsymbol{v}_h \, \mathrm{d}\Omega + \int_\Gamma q_h \rho_h \boldsymbol{v}_h \cdot \boldsymbol{n} \, \mathrm{d}\Gamma = 0 \tag{50}$$

and

$$\forall \boldsymbol{\omega}_h \in \mathcal{M}_h^d :$$

$$\begin{aligned}
&-\int_\Omega \nabla_s \boldsymbol{\omega}_h : \rho_h \boldsymbol{v}_h \otimes \boldsymbol{v}_h \, \mathrm{d}\Omega + \int_\Gamma (\boldsymbol{\omega}_h \otimes \boldsymbol{n})_s : (\rho_h \boldsymbol{v}_h \otimes \boldsymbol{v}_h) \, \mathrm{d}\Gamma = \\
&-\int_\Omega \nabla_s \boldsymbol{\omega}_h : \left(-p_h \hat{\boldsymbol{I}} + \hat{\boldsymbol{\sigma}}_h\right) \, \mathrm{d}\Omega + \int_\Gamma (\boldsymbol{\omega}_h \otimes \boldsymbol{n})_s : \left(-p_h \hat{\boldsymbol{I}} + \hat{\boldsymbol{\sigma}}_h\right) \, \mathrm{d}\Gamma \\
&+\int_\Omega \boldsymbol{\omega}_h \cdot \boldsymbol{F}_h \, \mathrm{d}\Omega + \int_\Omega \boldsymbol{\omega}_h \cdot \rho_h \boldsymbol{g} \, \mathrm{d}\Omega,
\end{aligned} \tag{51}$$

For the spatial approximation we use the $Q_2 - Q_1$ Taylor-Hood element, that satisfies the inf-sup condition (Donea and Huerta (2003); Gresho and Sani (1998)), and provides a continuous, piecewise bi-quadratic polynomial approximation for the velocity and a continuous, piecewise bi-linear approximation for the density.

3.2 Linearization

The discrete problem (50) and (51) is a nonlinear system of equations with respect to the solution variables ρ_h and $\boldsymbol{v}_h$. To solve it, a Newton-Raphson method is used. Starting from some arbitrary initial guess, a sequence of numerical approximations is built such that $\forall n = 0, 1, 2, ..., N$,

$$\rho_h^{n+1} \approx \rho_h^n + \delta\rho_h^n, \tag{52}$$

$$\boldsymbol{v}_h^{n+1} \approx \boldsymbol{v}_h^n + \delta\boldsymbol{v}_h^n. \tag{53}$$

The expansions (52) and (53) are substituted into the discrete weak formulation (50) and (51) and the terms of order $\mathcal{O}\left(\delta\rho_h^n, \delta\boldsymbol{v}_h^n\right)$ or higher are neglected.

3.3 Linear Algebra Solvers

At the end of each stage of the Newton-Raphson iterative procedure, the following linear system of algebraic equations is obtained

$$\mathbf{M}\left(\rho_h^n, \boldsymbol{v}_h^n\right)\delta\mathbf{x}_h^n = \boldsymbol{r}\left(\rho_h^n, \boldsymbol{v}_h^n\right), \tag{54}$$

where $\mathbf{M}\left(\rho_h^n, \boldsymbol{v}_h^n\right)$ and $\boldsymbol{r}\left(\rho_h^n, \boldsymbol{v}_h^n\right)$ are a sparse nonsymmetric tensor and residual vector respectively and $\delta\mathbf{x}_h^n = \left(\delta\rho_h^n, \delta\boldsymbol{v}_h^n\right)^{\mathrm{T}}$ is the nodal vector of unknown corrections. The direct methods implemented in either Unsymmetric Multifrontal Sparse LU Factorization Package (UMFPACK) (Davis (2004)) or Multifrontal Massively Parallel Sparse Direct Solver (MUMPS) (Amestoy et al. (1998)) are used to solve the linear system (54).

3.4 Implementation Details

The linearized discrete weak formulation of governing equations along with appropriate boundary conditions, iterative procedures, and other related routines have been implemented in the Open-Source Fuel Cell Simulation Toolbox (OpenFCST, Secanell et al. (2014)). OpenFCST is an open-source, finite element method based, multi-dimensional mathematical modeling software for polymer electrolyte fuel cells. The primary goal of this software is to develop a platform for collaborative development of fuel cell mathematical models. The linear solvers and finite element routines are provided by the finite element library deal.II (Bangerth et al. (2007)). The program can run in either serial or parallel mode (using the MPI protocol).

4 In-Plane and Through-Plane Permeability Measurements

Equations (39)-(46) governing the fluid flow in channels and porous media include two porous media-related parameters, which are the permeability tensor, $\hat{\boldsymbol{K}}$, and nonlinear Forchheimer correction tensor, $\hat{\boldsymbol{\beta}}$. Through-plane and in-plane components of these two tensors have been measured by many research groups. For fuel cell diffusion media, through-plane and in-plane properties have been measured

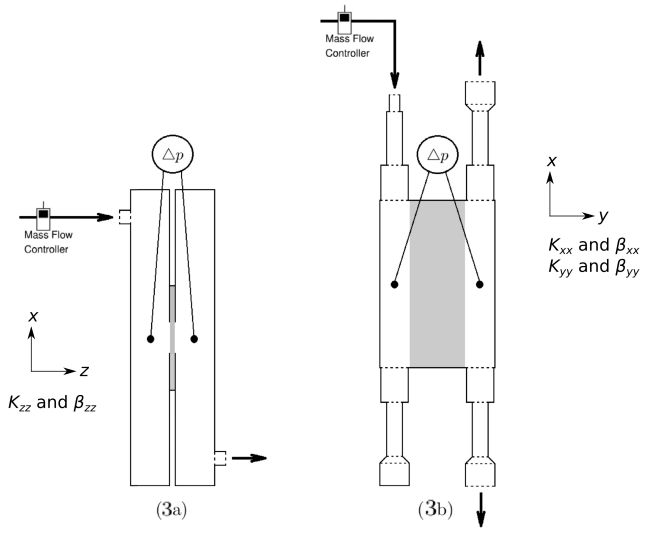

Fig. 3 Schematic view of the through-plane permeability experimental setup (3a) and in-plane permeability experimental setup (3b) used in Mangal et al. (2014) and Mangal et al. (2015).

for example by Gostick et al. (2006); Ismail et al. (2010, 2009); Orogbemi et al. (2018); Gurau et al. (2007); Tamayol et al. (2012); Pant et al. (2012); Carrigy et al. (2013); Mangal et al. (2014), and Mangal et al. (2015). In this study, the experimental setup in Mangal et al. (2014) and Mangal et al. (2015) is analyzed. The schematic representations of both through-plane and in-plane permeability experimental setups are shown in Figure 3. The porous layer is coloured in grey and the inlets and outlets of the channels are marked by arrows. For the in-plane experiments, a strip of porous media of dimensions 1×5 cm^2 was placed between two stainless steal plates that formed the channels. Porous media compression was controlled by using stainless steal shims between plates, such that the gap between plates was well known. In the experimental data in the paper, the porous media was compressed between shims with a thickness of 270.23 μm. For through-plane experiments, three GDL samples of dimension 20×25 mm^2 were stacked together and sandwiched within a lamination sheet with a hole of 9.5 mm in diameter to allow the gas to pass through the porous media.

In-plane and through-plane experiments of Mangal et al. (2014) and Mangal et al. (2015) involved varying mass flow rates, $\dot{m}$ $\left[\text{kg s}^{-1}\right]$, and recording the respective pressure drop across the porous media, Δp [Pa]. These values were used to evaluate the in-plane and through-plane components of the permeability tensor, $\hat{\boldsymbol{K}}$. The nonlinear Forchheimer correction tensor, $\hat{\boldsymbol{\beta}}$, is not estimated here since, as it will later be discussed, non-uniform flow in the channel is observed at high flow rates leading to channel effects on the pressure gradient. A detailed description of the in-plane and through-plane experimental setups are given in references Mangal et al. (2014) and Mangal et al. (2015), respectively.

Most experimental studies, e.g., Gostick et al. (2006); Ismail et al. (2010, 2009); Orogbemi et al. (2018); Gurau et al. (2007); Tamayol et al. (2012); Pant et al.

(2012); Carrigy et al. (2013); Mangal et al. (2014), and Mangal et al. (2015), recovered the tensors $\hat{\boldsymbol{K}}$ and $\hat{\boldsymbol{\beta}}$ by assuming the three-dimensional systems in Figure 3 could be treated as a one-dimensional porous layer thereby neglecting any channel, boundary layer, inertial, and wall effects. Under the assumptions above, a one-dimensional steady-state compressible and isothermal Darcy-Forchheimer model was used to couple measurable flow parameters with unknown permeability coefficients. The model itself can be obtained from the more general multi-dimensional equations (29), (30), and (31) by neglecting inertia and shear stress terms. Let us consider only the x-direction (Mangal et al. (2014)):

$$\frac{dp}{dx} = -\frac{\mu}{K_{xx}} v - \beta_{xx} \rho v^2 \tag{55}$$

where p is the phase-averaged pressure, and v is the x-component of the phase-averaged velocity. The mass flux is defined as:

$$\boldsymbol{N} = \rho \boldsymbol{v} \tag{56}$$

where $\boldsymbol{N}$ is measured in kg m^{-2} s^{-1}. Assuming that the fluid is an ideal gas, and considering equation (56) in the x-direction, equation (55) can be re-written as (Mangal et al. (2014)):

$$\frac{dp}{dx} = -\frac{1}{\rho}\left(\frac{\mu}{K_{xx}} N + \beta_{xx} N^2\right) = -\frac{RT}{p}\left(\frac{\mu}{K_{xx}} N + \beta_{xx} N^2\right) \tag{57}$$

where N is the mass flux in the x-direction. Since no chemical reactions are considered in the present model, the mass flux is constant. Thus, integrating from $x = 0$ to L, and $p = p_1$ to p_2, equation (57) becomes the compressible Darcy-Forchheimer equation:

$$\frac{p_1^2 - p_2^2}{2RTL} = \frac{\mu}{K_{xx}} N + \beta_{xx} N^2 \tag{58}$$

This equation differs from the equation that would be obtained using the one-dimensional version of equation (40) after canceling inertial, gravitational, and viscous effects, and with the stable pair $<\rho>$, $<\boldsymbol{v}>^{\mathrm{f}}$ (as shown in Table 1), which would lead to:

$$\frac{p_1^2 - p_2^2}{2RTL} = \frac{\mu}{K_{xx}} \varepsilon N + \beta_{xx} \varepsilon^2 N^2 \tag{59}$$

Since equation (59) is different from the most commonly used expression in the literature Feser et al. (2006); Gostick et al. (2006); Gurau et al. (2007); Ismail et al. (2009), i.e., equation (58), the reported permeability data in the literature must be corrected to be used in the proposed model as follows:

$$\hat{\boldsymbol{K}}_{\text{model}} = \varepsilon \hat{\boldsymbol{K}}_{\text{experiment}} \tag{60}$$

Depending on the averaging solution pair used, a similar correction might be needed for other implementations of equation (40) such as those used in commercial software and used in fuel cell simulations, e.g., Pharoah (2005); Park and Li (2007); Nguyen et al. (2004); Park and Li (2011); Saha et al. (2008); Saha and Oshima (2012); Salahuddin et al. (2013); Salahuddin and Oshima (2013); Qin et al. (2018); Zhang et al. (2019b).

5 Computational Studies

In this section, first a discussion on the channel/porous media interface coupling, and the subsequent stability issues with the formulations proposed in section 2.4 is presented. Then, the through-plane and in-plane experimental setups from Mangal et al. (2014, 2015), and Xu (2019) are studied in order to verify that the assumptions required to estimate the permeability using a one-dimensional model are valid. Finally, to illustrate the capabilities of the model, the fluid flow pattern in a gas diffusion media under a serpentine and an interdigitated fuel cell gas channel is studied.

5.1 Validation of the Computational Code

In order to guarantee the correct implementation of the developed fluid flow solver, the well-known lid-driven cavity flow benchmark problem is first solved. Appendix A provides a summary of the validation results.

5.2 In-plane Permeability Setup in Two Dimensions

The effects of the choice of solution variables on the accuracy of the numerical solution in the computational domain are studied in this example. The two-dimensional computational domain is composed of two gas channels and a porous layer. The domain is shown in Figure 4(a). The porous layer is colored in green, and the inlet and outlet gas channels are coloured in red and blue, respectively. The channel inlet and outlets are marked by arrows. The porous media is considered to be a Toray 090 20% PTFE sample, with a porosity of 0.7, and a permeability of 6×10^{-12} m^2, taken from Mangal et al. (2014). Nitrogen at a temperature of 298 K is used as the fluid.

No-slip velocity boundary conditions are applied at all solid walls of the computational domain. A parabolic velocity profile with a maximum value of $v_x = 1$ m s^{-1} is prescribed at the inlet of the high-pressure channel (i.e., red channel in Figure 4(a)), which corresponds to $Re = 640$. A relative pressure of 0 Pa and vanishing normal components of shear stresses are assumed at both outlets of the low-pressure gas channel (i.e., blue channel in Figure 4(a)).

The system of governing equations (39)-(46) is solved in serial in an Intel(R) Xeon(R) E5-2690 v2 CPU with a clock speed of 3.00 GHz, and the average computational time is 1 minute. The computational grid for this study (Figure 4(b)) contains 7×10^4 degrees of freedom (DOFs). A grid independence study shows that pressure and velocity solutions change less than 1% compared to a once globally refined grid with 1.4×10^5 DOFs.

5.2.1 The Effect of Channel - Porous Media Interface

Section 2.4 highlighted that there are four possible choices for the averaged solution variables in porous media, see Table 1. The choice of solution variables affects the stability of the numerical solution. In this section, results using the different formulations are discussed.

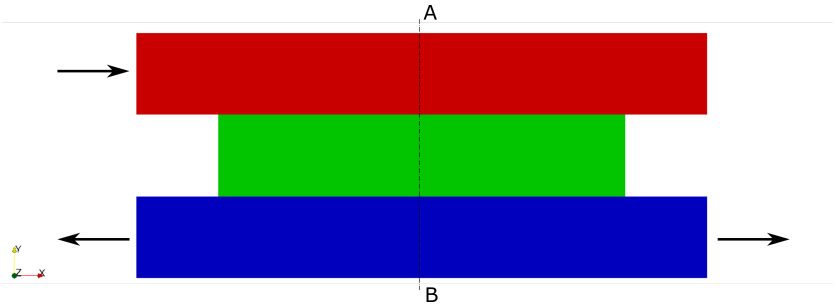

(a) Geometry of the in-plane permeability setup

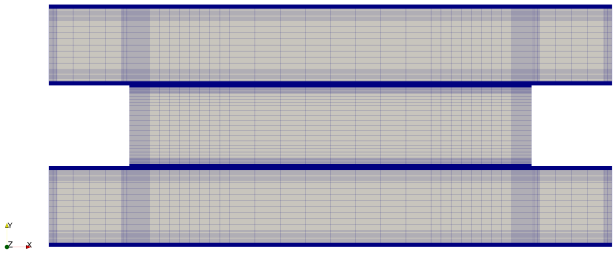

(b) Computational mesh

Fig. 4 (a) Geometry of the in-plane permeability setup, and (b) computational mesh.

Solving the system of governing equations (39)-(46) in terms of the $\left(<\rho>, <\boldsymbol{v}>^{\mathrm{f}}\right)$ solution pair in the porous layer results in a stable and non-oscillatory numerical solution. The pressure and velocity fields are shown in Figure 5(a) and 5(b), respectively. The pressure field depicted in Figure 5(a) shows that most of the pressure drop occurs across the porous layer.

Solving the system of governing equations (39)-(46) with either $\left(<\rho>^{\mathrm{f}}, <\boldsymbol{v}>\right)$ or $\left(<\rho>^{\mathrm{f}}, <\boldsymbol{v}>^{\mathrm{f}}\right)$ solution pairs in the porous domain results in either an unstable or a highly oscillatory numerical solution in both gas channels and porous layer. According to Table 1, in order to satisfy mass and momentum conservation, both combinations $\left(<\rho>^{\mathrm{f}}, <\boldsymbol{v}>\right)$ and $\left(<\rho>^{\mathrm{f}}, <\boldsymbol{v}>^{\mathrm{f}}\right)$ must introduce a jump in the density field at the interface between gas channels and porous medium. Since the solution approximation is assumed to be a continuous function, this jump is difficult to capture and it tends to propagate back into the gas channels resulting in an unstable solution. Therefore, these pairs of variables should not be used as they do not produce a stable solution.

The remaining set, i.e., $(<\rho>, <\boldsymbol{v}>)$, results in a stable solution, however, oscillations and a discontinuity in the normal component of the velocity can be observed at the channel/porous media interface (Figure 5(d)). The numerical solution for the two stable solution variable pairs, plotted over the channel centerline AB (Figure 4(a)), is shown in Figure 6(a). When the pair $(<\rho>, <\boldsymbol{v}>)$ is used (*Pair B*, red dashed line), the numerical approximation of the normal velocity component, v_y, is discontinuous at the channel/porous layer interface. The ratio of the two velocities in the porous media (*Pair A*, black solid line, and *Pair B*, red dashed

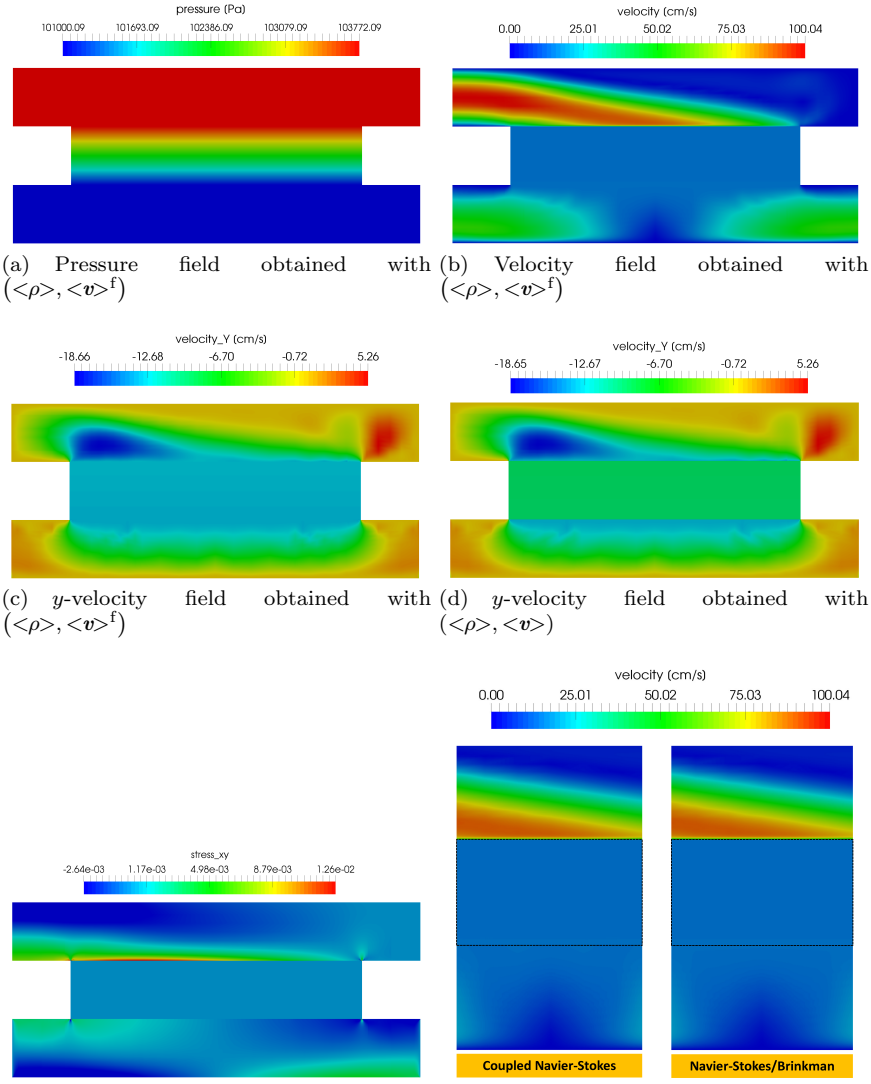

(a) Pressure field obtained with $(<\rho>, <\boldsymbol{v}>^{\mathrm{f}})$

(b) Velocity field obtained with $(<\rho>, <\boldsymbol{v}>^{\mathrm{f}})$

(c) y-velocity field obtained with $(<\rho>, <\boldsymbol{v}>^{\mathrm{f}})$

(d) y-velocity field obtained with $(<\rho>, <\boldsymbol{v}>)$

(e) Tangential component of the stress tensor obtained with $(<\rho>, <\boldsymbol{v}>^{\mathrm{f}})$

(f) Velocity field obtained with coupled NS and NS/Brinkman

Fig. 5 (a)-(c) Distribution of pressure, velocity and y-velocity obtained with $(<\rho>, <\boldsymbol{v}>^{\mathrm{f}})$, (d) y-velocity distribution obtained with $(<\rho>, <\boldsymbol{v}>)$, (e) Tangential component of the stress tensor obtained with $(<\rho>, <\boldsymbol{v}>^{\mathrm{f}})$, and (f) Comparison of velocity profiles in the central region with the fully coupled Navier-Stokes equations and the Navier-Stokes/Brinkman equations (porous media marked with a dashed box).

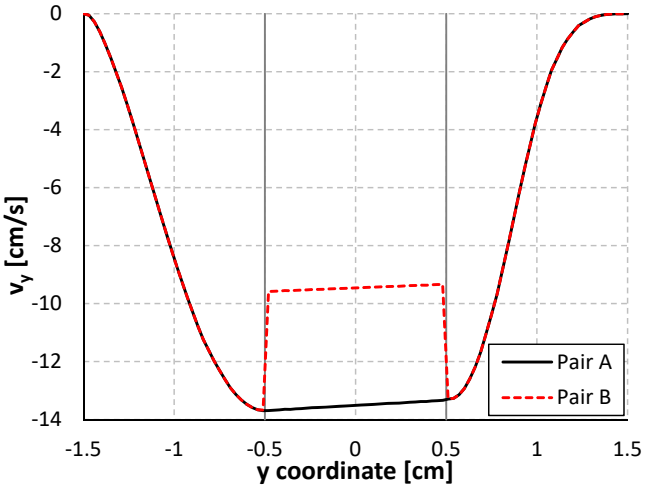

(a) Velocity y-component

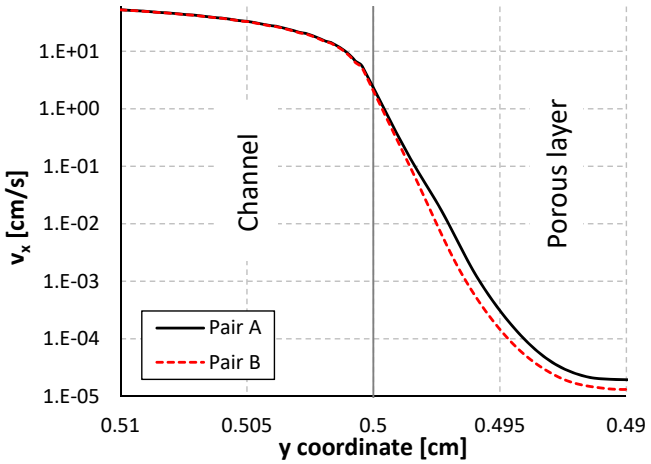

(b) Velocity x-component at the channel/porous medium interface

Fig. 6 (a) Normal velocity distribution along the symmetry line AB for two pairs of solution variables A: $(<\rho>, <\boldsymbol{v}>^{\mathrm{f}})$, and B: $(<\rho>, <\boldsymbol{v}>)$, and (b) tangential velocity distribution at the channel/porous layer interface in the symmetry line AB.

line) is the porosity. The difference in velocity is due to the averaging method used. The distribution of the tangential velocity component, v_x, does not show any discontinuities and/or oscillations, and the pressure distribution is identical in both simulations (Figure 5(a)). The convergence of the nonlinear solver and the computational time are similar between both pairs.

The continuity of the tangential component of the velocity at the channel-porous medium interface has been studied in literature (e.g., Beavers and Joseph (1967); Dobberschütz (2015); El-Jarroudi and Er-Riani (2018)). Numerical mod-

els that consider Stokes or Navier-Stokes equations in the channel and Darcy's law in the porous medium require the imposition of the Beavers-Joseph condition for the jump in the tangential velocity component at the channel/porous medium interface (Beavers and Joseph (1967)). Since the current study considers the fully-coupled Navier-Stokes equations in the channel and porous medium, continuity of the velocity components is naturally imposed by the governing equations for the stable pair $\left(<\rho>, <\boldsymbol{v}>^{\mathrm{f}}\right)$. Figure 5(e) displays the tangential component of the stress tensor, showing a large value close to the channel/porous medium interface. The model used in this study is able to capture the non-zero value of the tangential velocity component at the channel/porous medium interface, as well as the continuous transition of the velocity field from the channel region to the porous layer (Figure 6(b)).

The in-plane permeability simulation is repeated using the compressible Navier-Stokes equations in the channels and the Brinkman equation in the porous media. Comparison of the velocity profiles in the vicinity of the symmetry line AB (Figure 4(a)) obtained with the fully coupled Navier-Stokes equations and the Navier-Stokes/Brinkman equations is shown in Figure 5(f). For this particular problem, no significant changes in the velocity profiles are observed, and the number of iterations of the nonlinear solver is identical. Therefore, the more accurate fully coupled Navier-Stokes equations are recommended.

In summary, the combination of solution variables $\left(<\rho>, <\boldsymbol{v}>^{\mathrm{f}}\right)$ generates a stable and non-oscillatory numerical approximation and therefore it is the most appropriate pair of volume-averaged variables to study channel/porous media problems.

5.3 Study of the Experimental Through-Plane Permeability Setup

In order to study channel and inertial effects on the through-plane setup developed by Pant et al. (2012), a three-dimensional model of the through-plane permeability experimental setup is developed. For simplicity, only half of the geometry is considered due to its symmetry with respect to the xz-plane. The computational domain is shown in Figure 7. The porous layer is shown in green, whereas the high pressure and low pressure channels are colored in blue and red, respectively. The lamination sheets used in the experimental setup are also considered in the geometry. The fluid considered is nitrogen with a density and dynamic viscosity of $\rho = 1.14$ kg m^{-3} and $\mu = 1.782 \times 10^{-5}$ Pa s, respectively. These properties correspond to a constant temperature of $T = 298$ K and an outlet pressure of $p_{out} = 101000$ Pa. The porous material is a GDL Toray 090 20% PTFE sample with a porosity of $\varepsilon = 0.7$. The same boundary conditions as in Section 5.2 are used with the exception of the inlet velocity, which is given by

$$v_y\Big|_{\Gamma_{\mathrm{in}}} = v_z\Big|_{\Gamma_{\mathrm{in}}} = 0, \qquad v_x\Big|_{\Gamma_{\mathrm{in}}} = \frac{\dot{Q}}{A}\Big|_{\Gamma_{\mathrm{in}}}, \tag{61}$$

where $\dot{Q}$ is the volume flow rate measured experimentally by a mass flow controller, and A is the cross-sectional area. A no-slip boundary condition for velocity is imposed on the channel and GDL walls. A perfect slip boundary condition for velocity is imposed at the symmetry plane, with $\boldsymbol{v} \cdot \boldsymbol{n} = v_y = 0$.

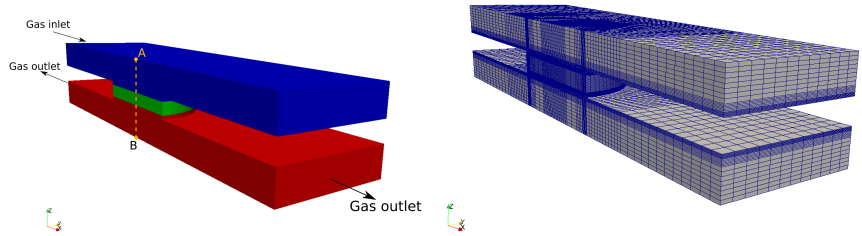

(a) Geometry of the through-plane permeability setup

(b) Computational mesh of the through-plane permeability setup

Fig. 7 Geometry and computational mesh used in the through-plane simulations.

Table 2 In-plane and through-plane values of permeability tensor $\hat{\boldsymbol{K}}$ obtained from experimental and numerical data

	$K_{xx} \times 10^{-12}$ [m^2]	$K_{yy} \times 10^{-12}$ [m^2]	$K_{zz} \times 10^{-12}$ [m^2]
Experimental (1D model)	6.645	6.645	4.62
Calibrated (3D model)	7.128	7.128	4.05

The system of governing equations (39)-(46) is solved in parallel using 7 cores in an Intel(R) Xeon(R) E5-2690 v2 CPU with a clock speed of 3.00 GHz, and the average computational time is 1 hour. The computational grid for the through-plane permeability study (Figure 7(b)) contains $4.3{\times}10^5$ DOFs. A grid independence study shows that the pressure drop changes less than 0.4% compared to a once globally refined grid with $9{\times}10^5$ DOFs.

5.3.1 Through-plane permeability parametric study

A series of experiments were performed in Mangal et al. (2015) and Xu (2019) to obtain the pressure drop across the porous media in the z-direction, Δp, at varying mass flow rates, $\dot{m}$, for a Toray 090 20% PTFE sample. The pressure was measured at the top and bottom walls of the high and low pressure channels (points A and B in Fig. 7(a)), respectively. To estimate the porous media permeability, numerical simulations with a constant flow rate of 1.0 SLPM are performed with varying values of K_{zz}, until the pressure drop across the porous medium coincides with the experimental data reported in Mangal et al. (2015) and Xu (2019). The pressure variation along the y-direction line $\bar{AB}$ (dashed vertical line in Figure 7(a)) is considered. The pressure drop for varying permeability values at $Q = 1$ SLPM is displayed in Fig. 8(a). The value of $K_{zz} = 4.05 \times 10^{-12}$ m^2 provides the best fit.

After estimating the through-plane permeability, simulations with varying flow rates from 0 to 1 SLPM are performed and compared to experimental data in Mangal et al. (2015) and Xu (2019). Results obtained in the experiments (orange squares) with the error bars for the measurements, and the numerical results (solid black line) using data in Table 2 are displayed in Figure 8(b). The figure shows excellent agreement between model and experimental results.

Most experimental studies, e.g., Feser et al. (2006); Gostick et al. (2006); Gurau et al. (2007); Ismail et al. (2009); Hussaini and Wang (2010); Ismail et al. (2010, 2011); Pant et al. (2012); Carrigy et al. (2013); Mangal et al. (2014, 2015), used equation (58) to extract the permeability coefficient from the experimental results thereby ignoring any channel effects. In order to assess the validity of the 1D model to extract a permeability value, the same simulation is performed with the permeability value obtained using equation (58) with β_{zz} set to zero and once K_{zz} has been corrected by porosity as discussed in Section 4. Figure 8(b) shows the simulations cannot reproduce the experimental values with the permeability obtained from equation (58) indicating channel effects must be considered, especially at high flow rates. The error on the permeability estimation leads to an error of 9% at 1 SLPM. This error increases with increasing flow rate values, which indicates that predictions of the Forchheimer tensor components might not be accurate for 1D models that consider a Darcy-Forchheimer regime in the porous material unless channel-porous media effects are minimized.

Velocity and pressure distributions in the yz symmetry plane at two different gas flow rates are shown in Figure 9. Most of the pressure drop occurs across the porous medium, as shown in Figures 9(a) and 9(c). At low flow rates, the gas enters the porous material without a complex flow pattern in the high pressure channel (Figure 9(b)). At increased flow rates however, a complex flow pattern develops in the high-pressure channel, as depicted in Figure 9(d). This complex flow pattern is likely responsible for the discrepancy between permeability predictions in the proposed experimental setup.

5.4 Study of an Experimental In-Plane Permeability Setup

The numerical model is used to extract the in-plane permeability of the GDL sample, i.e., K_{xx} and K_{yy}, by simulating the three-dimensional geometry of the experimental setup in references Gostick et al. (2006); Mangal et al. (2014); Xu (2019). In this case, the geometry is symmetric with respect to the xy-plane and therefore only half of the domain is considered. The computational domain is shown in Figure 10. The porous layer is again colored in green, the high pressure channel in blue, and the low pressure channel in red. The same boundary conditions as in Section 5.3 are used with the exception of the lateral GDL walls (i.e., walls parallel to the YZ-plane), where a perfect slip boundary condition for velocity is imposed.

The system of governing equations (39)-(46) is solved in parallel using 7 cores in an Intel(R) Xeon(R) E5-2690 v2 CPU with a clock speed of 3.00 GHz, and the average computational time is 45 minutes. The computational grid for the in-plane permeability study (Figure 7(b)) contains 6.2×10^5 DOFs, which is enough to achieve a grid independent solution.

5.4.1 In-plane permeability parametric study

The experimental results from references Mangal et al. (2014) and Xu (2019) of varying mass flow rates for a Toray 090 20% PTFE sample are analyzed next. The in-plane components of the permeability tensor, i.e., K_{xx} and K_{yy}, are estimated by performing a parametric study with varying permeability values at $Q = 0.6$

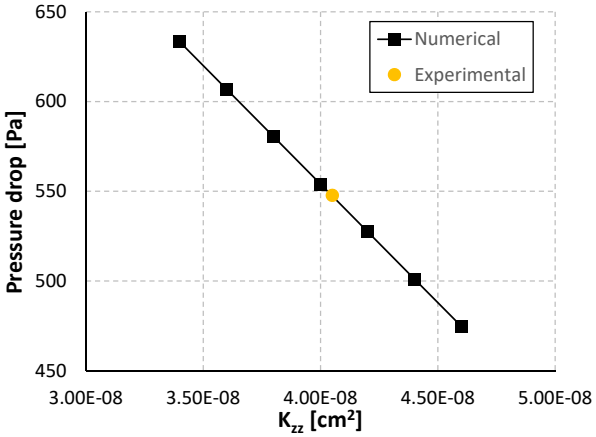

(a) Pressure drop for different permeability values at $Q = 1$ SLPM

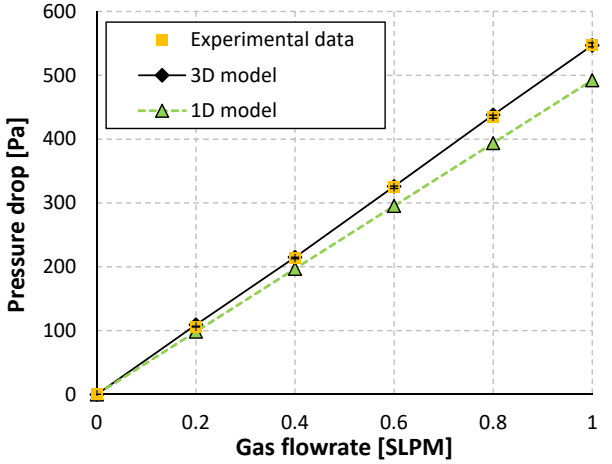

(b) Experimental and numerical data of pressure drop at varying flow rates

Fig. 8 (a) Pressure drop obtained in the numerical simulations for different through-plane permeability values at $Q = 1$ SLPM, and (b) comparison between numerical and experimental results for the through-plane permeability setup.

SLPM and selecting the permeability value that reproduces the pressure drop between channels. In the experiments of Mangal et al. (2014) and Xu (2019), pressure was measured at the top wall of the channels (points A and B in Figure 10(a)). The pressure is measured at the center of the channels in the numerical simulations since the pressure variations in the channel are negligible. The resulting in-plane permeability values are $K_{xx} = K_{yy} = 7.128 \times 10^{-12}$ m^2.

Once the in-plane permeability components are estimated, a series of simulations with varying flow rate values from 0 to 0.6 SLPM are performed. Results obtained in the experiments in references Mangal et al. (2014) and Xu (2019), and

(a) Pressure distribution, $Q = 0.2$ SLPM

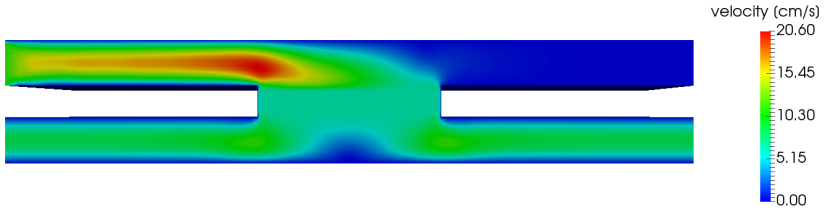

(b) Velocity distribution, $Q = 0.2$ SLPM

(c) Pressure distribution, $Q = 1.0$ SLPM

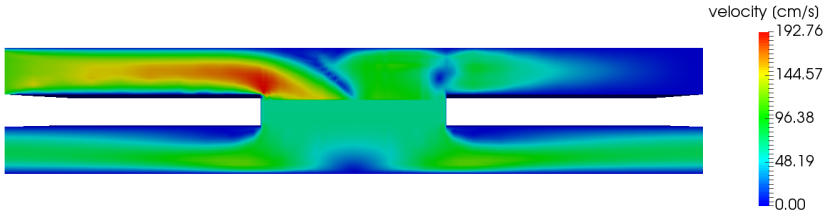

(d) Velocity distribution, $Q = 1.0$ SLPM

Fig. 9 Pressure and velocity profiles for (a)-(b) $Q = 0.2$ SLPM, and (c)-(d) $Q = 1.0$ SLPM.

simulations are displayed in Figure 11. The simulations are also performed considering the fitted permeability value obtained with the 1D model in equation (58). At high flow rates, the discrepancy between the predicted pressure drop using the 3D estimated and the 1D estimated values can be as high as 8%.

Figures 12(a) and 12(b) show the pressure and velocity distributions for the $Q = 0.5$ SLPM case in the xy symmetry plane. Most of the pressure drop occurs along the porous media, as in the through-plane study. An interesting feature is the predicted high gas velocity in the porous material due to the reduced cross-sectional area of the GDL. This high velocity in the porous material results in a

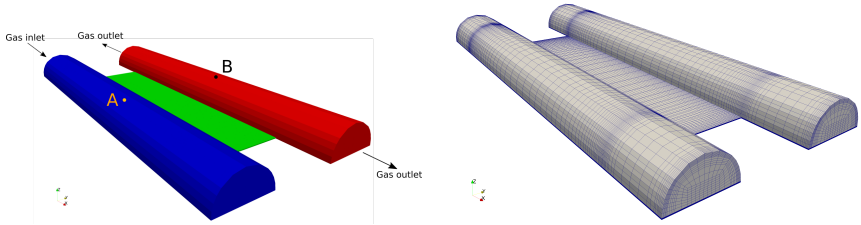

(a) Geometry of the in-plane permeability setup (b) Computational mesh of the in-plane permeability setup

Fig. 10 Geometry and computational mesh used in the in-plane simulations.

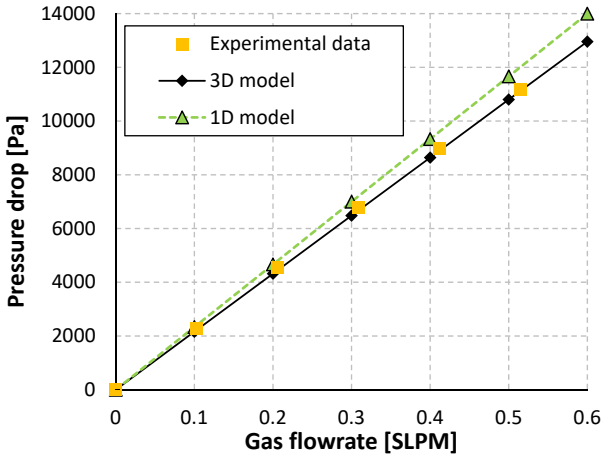

Fig. 11 Comparison between numerical and experimental results for the in-plane permeability setup.

jet-like flow pattern at the low pressure channel resulting in several recirculations even at low flow rates of 0.5 SLPM. Therefore, channel effects are important even at moderate flow rates and are likely responsible for the discrepancy between the in-plane permeabilities obtained with a 1D and a 3D model, i.e., 6.645×10^{-12} m^2 vs. 7.128×10^{-12} m^2. These results also cast a large doubt regarding Forchheimer permeability predictions in literature using a 1D model as channel/porous media interactions are clearly affecting results at high flow rates. When the gas enters the low-pressure channel, it recirculates in the direction parallel to the yz-plane (Figure 12(c)), and these vortexes tend to vanish towards the channel exit. Extremely fine meshes are required to capture this complex flow pattern for flow rate values larger than $Q = 0.6$ SLPM.

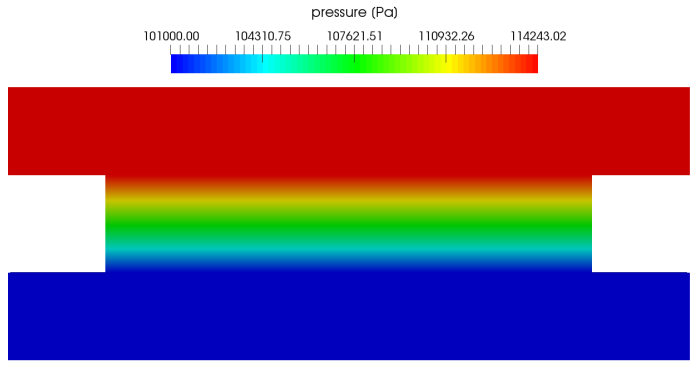

(a) Pressure distribution

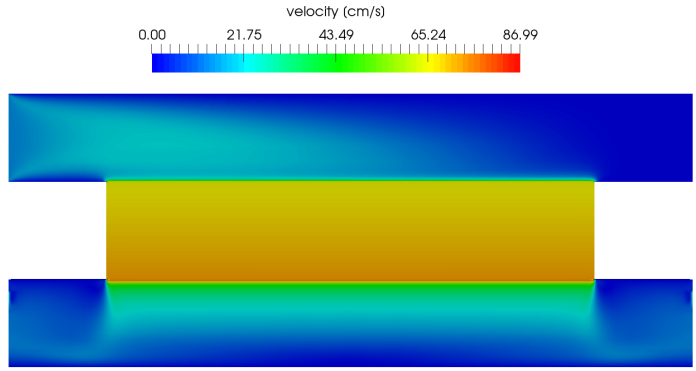

(b) Velocity distribution

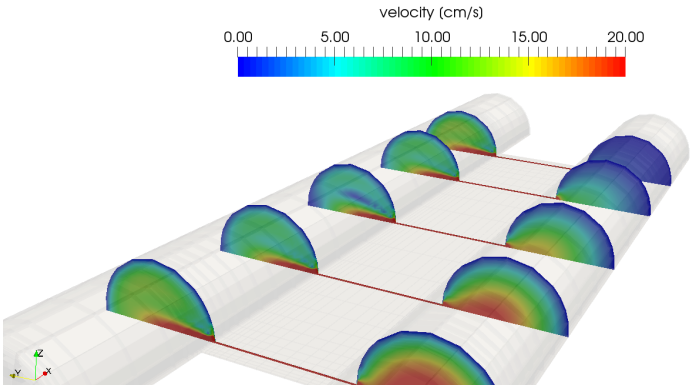

(c) Velocity profile slices along the low-pressure channel (left)

Fig. 12 (a) Pressure and (b) velocity distributions in the XY symmetry plane, and (c) velocity profiles in the YZ-planes along the high and low-pressure channels.

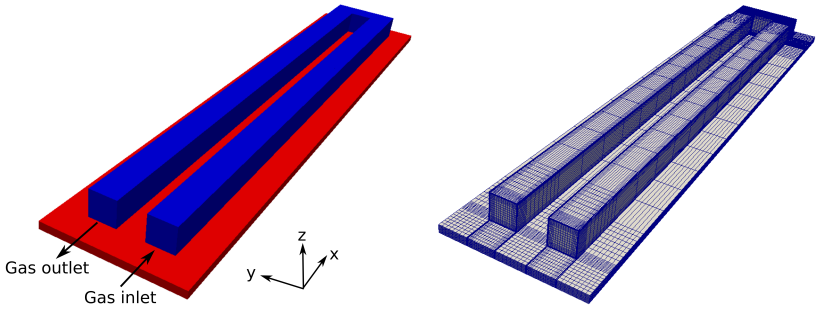

(a) Geometry (b) Computational mesh

Fig. 13 (a) Geometry and (b) computational mesh used for the simulation of a fuel cell serpentine channel and a gas diffusion layer.

5.5 Study of a Three-Dimensional Fuel Cell Serpentine Channel

Serpentine gas channels mounted on a permeable gas diffusion layer are one of the most commonly used channel layouts in fuel cells. The pressure difference between straight sections of the serpentine channels leads to a cross flow induced in the GDL, which facilitates oxygen transport to the catalyst layer. The aim of this test case is to predict the fluid flow occurring through the GDL under the rib of a serpentine channel.

Several numerical studies in literature have used a compressible fluid flow solver to study mass transport phenomena in fuel cell serpentine channels (Nguyen et al. (2004); Hashemi et al. (2012); Salahuddin and Oshima (2013); Zhang et al. (2019a)); however, the above-mentioned studies did not include any discussion on volume-averaging of the governing equations in the porous media, considered the porous media to be an isotropic material, and used permeability values from literature obtained with one-dimensional models (Feser et al. (2006); Gostick et al. (2006); Ismail et al. (2009, 2010); Carrigy et al. (2013); Mangal et al. (2014, 2015)). Therefore, the advantages of using a realistic value for the permeability of the GDL, and the consideration of porous media anisotropy are highlighted.

The considered geometry for the channel consists of two straight channels with a cross-sectional area of 1×1 mm^2 and a length of 22 mm, connected at one end (similar to the geometry used by Pharoah (2005)). The channels are mounted on a Toray 090 20%PTFE GDL sample, as shown in Figure 13(a). The serpentine channel and the GDL are displayed in blue and red, respectively. Parameters characterizing the channel and GDL geometries are detailed in Table 3, as well as the ambient conditions and properties of nitrogen. The permeability values for the GDL have been obtained in Sections 5.3 and 5.4, and are detailed in Table 2.

The gas flow rate at the inlet is varied between $Q = 0.09$ and 0.37 SLPM corresponding to Reynolds numbers between 100 and 400. This range of Reynolds numbers is usually chosen in numerical studies (Pharoah (2005); Salahuddin and Oshima (2013), although gas flow rates in an operating fuel cell can be much higher. At higher flow rates, the proposed model is not able to find a steady-state solution due to the complexity of the flow pattern as also observed by Pharoah

Table 3 Geometry, operating conditions and gas properties for the serpentine channe simulation

Paraneter	Value	Units
Channel length	22	mm
Channel width	1	mm
Channel height	1	mm
Channel pitch	1	mm
GDL thickness	290 (Xu (2019))	μm
GDL porosity	0.7 (Xu (2019))	-
Pressure	101000	Pa
Temperature	298	K
Nitrogen density at channel outlet	1.14	kg m^{-3}
Nitrogen dynamic viscosity at channel outlet	1.782×10^{-5}	Pa s

(2005). A constant pressure of 100 kPa is set at the channel outlet. A slip boundary condition for velocity is imposed at the lower wall of the GDL (parallel to the xy-plane), which represents the interphase between the GDL and the catalyst layer.

The system of governing equations (39)-(46) is solved in parallel using 9 cores in an Intel(R) Xeon(R) E5-2690 v2 CPU with a clock speed of 3.00 GHz, and the average computational time is 2 hours. The computational grid for the serpentine channel study (Figure 13(b)) contains 6.5×10^5 DOFs. A grid independence study shows that the pressure drop changes less than 2% compared to a once globally refined grid with 1.3×10^6 DOFs.

5.5.1 Effects of the GDL on the pressure drop in the channel

The effect of the presence of a GDL on the pressure drop in the gas channel is studied by considering the serpentine channel without GDL and with GDL. Figure 14 displays the pressure drop along the serpentine channel at varying gas flow rates. The pressure drop at a given mass flow rate is shown to be lower in the presence of the GDL, which has been previously observed in literature (Pharoah (2005); Saha and Oshima (2012); Park and Li (2011)). The difference in pressure drop can be as high as 11% at flow rates of 0.37 SLPM. Pharoah (2005) studied the pressure drop on the channel for varying permeability values and a Reynolds number of 100. For $K_{xx} = 10 \times 10^{-12}$ m^2 a pressure drop of 1625 Pa m^{-1} was predicted. In our numerical simulations, a pressure drop of 1710 Pa m^{-1} with an in-plane permeability of $K_{xx} = 7.128 \times 10^{-12}$ m^2 is obtained, which is in good agreement.

Three-dimensional pressure and velocity streamline distributions are depicted in Figures 15(a) and 15(b), respectively. The pressure field along the serpentine gas channel monotonically decreases from its inlet towards the outlet. The velocity field exposes the flow cross-over under the rib of a serpentine channel. Figure 15(c) provides the information on the velocity field over the GDL xy-plane at the bottom of the domain, i.e., $z = 0$, at the highest mass flow rate. For permeability values of $K_{xx} = 5 \times 10^{-12}$ m^2 and a GDL thickness of 250 μm, Pharoah (2005) predicted that approximately 5% of the inlet flow crosses the GDL under the land. Our model reveals that for a Toray 090 20%PTFE sample, this bypass is 4.3%, which is in agreement with the numerical simulations of Pharoah (2005). The bypass is calculated by computing the difference between the mass fluxes at the inlet

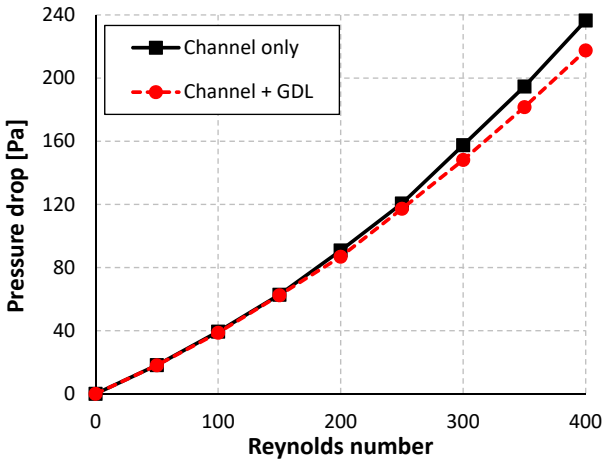

Fig. 14 Pressure drop in the serpentine gas channel at varying Reynolds numbers with and without a GDL.

and outlet faces (i.e., faces perpendicular to the x axis) in the first channel, and then dividing this difference by the mass flux at the inlet. For permeability values lower than 10^{-11} m^2, Pharoah (2005) observed that this bypass was the same for different flow rates. In our simulations, we also have found that the amount of flow bypassing under the land is constant for the considered flow rates.

The three-dimensional fuel cell serpentine channel simulation is repeated using the compressible Navier-Stokes equations in the channels and the Brinkman equation in the porous media. The resulting velocity profile in the porous media is displayed in Figure 15(d). Although there are no significant differences in the velocity distribution obtained with the fully coupled Navier-Stokes equations (Figure 15(c)), the resulting profile exhibits oscillations in the numerical solution. Moreover, the nonlinear solver, in this case, needs 7 iterations to converge, whereas the simulation with the fully coupled Navier-Stokes equations converges in just 2 iterations. These results indicate that considering the compressible Navier-Stokes equations in the channel coupled with the Brinkman equation in the porous media may lead to numerical instabilities for three-dimensional problems.

5.5.2 Effects of GDL anisotropy

The simulation considered in Section 5.5.1 is reproduced without taking into account the anisotropic nature of the porous material. Therefore, the permeability components in this case are all equal to the in-plane components in Table 2, i.e., $K_{xx} = K_{yy} = K_{zz} = 7.128 \times 10^{-12}$ m^2.

The difference in the predicted pressure drop along the channel varies less than 1% with respect to the results shown as a red dashed line with circle markers in Figure 14, which means that for fuel cell channels, the mass transport through the gas diffusion layer is governed by the in-plane component of the permeability tensor. This observation is in agreement with the work of Pharoah (2005); Hashemi et al. (2012); Salahuddin and Oshima (2013)).

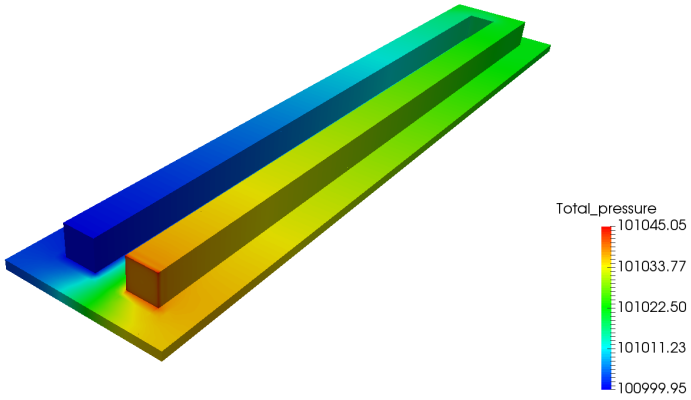

(a) Pressure distribution

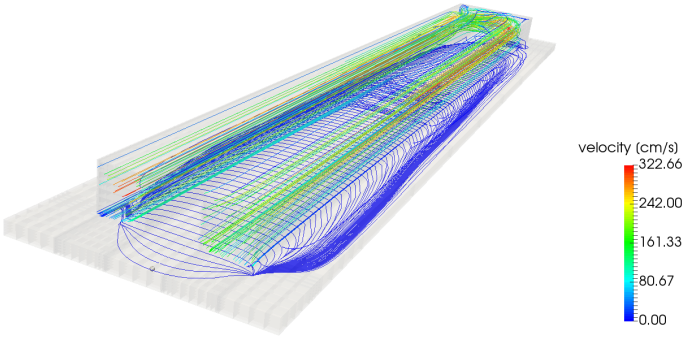

(b) Velocity streamlines

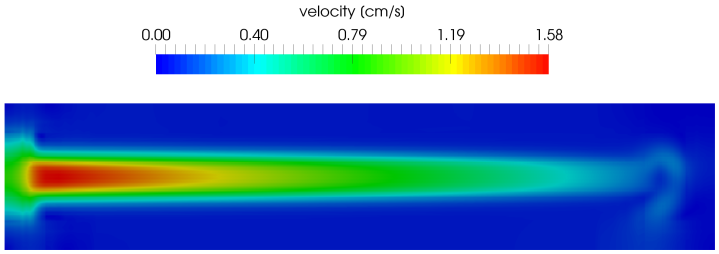

(c) Velocity profile in the plane $z = 0$

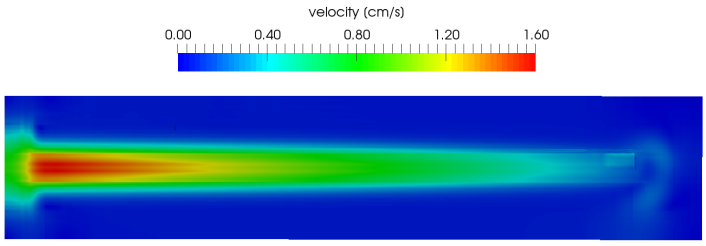

(d) Velocity profile in the plane $z = 0$ obtained with NS/Brinkman equations

Fig. 15 (a) Pressure and (b) velocity streamline distributions in the serpentine channel and GDL, (c) velocity profile in the XY-plane at the bottom of the domain ($z = 0$), and (d) velocity profile at $z = 0$ obtained with the Navier-Stokes/Brinkman equations.

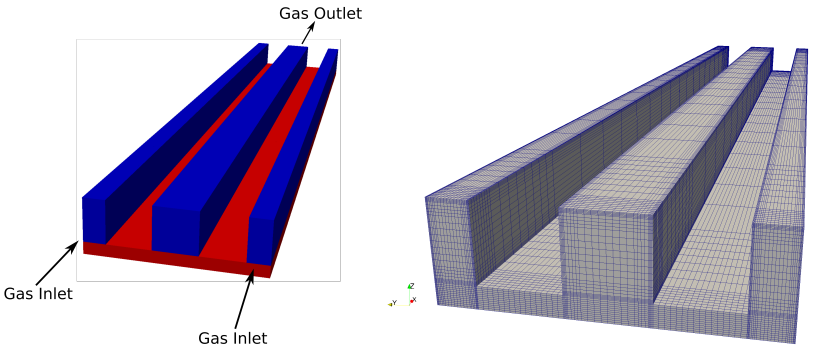

(a) Geometry (b) Computational mesh

Fig. 16 (a) Geometry and (b) computational mesh used for the simulation of a fuel cell interdigitated channel and a gas diffusion layer.

5.5.3 Interdigitated channel design

In serpentine channel designs for fuel cell flow fields the amount of gas bypassing the channel is small as already discussed in Section 5.5. An alternative to serpentine channels to enhance convective flow in the GDL is an interdigitated design, which forces the gas to flow through the GDL, thus improving the performance at the cost of increasing the pressure drop along the channels. This example considers an interdigitated channel design to quantify the pressure drop at different flow rates, and estimate the velocity inside the GDL.

The geometry considered in this section is depicted in Figure 16(a), with two inlet channels at both sides of an outlet channel. Due to the symmetry of the geometry, only half of the two inlet channels is used. The two inlet channels and the outlet channel have only one end open, as displayed in Figure 16, and they are connected only via the gas diffusion layer. Channel and GDL size, GDL type, and fluid properties are detailed in Table 3.

The system of governing equations (39)-(46) is solved in parallel using 9 cores in an Intel(R) Xeon(R) E5-2690 v2 CPU with a clock speed of 3.00 GHz, and the average computational time is 2 hours. The computational grid for the interdigitated channel study contains 5×10^5 DOFs (Figure 16(b)). A grid independence study shows that the pressure drop changes less than 0.6% compared to a once globally refined grid with 1×10^6 DOFs.

Pressure drop in the domain for the $Re = 400$ case, i.e., $Q = 0.37$ SLPM, which would correspond to a current density of 1.58 A cm^{-2} at a stoichiometry of 15, is depicted in Figure 17. Velocity slices along the channel direction (i.e., x-direction) reveal that the gas enters the two lateral channels, it diffuses through the GDL, and it finally exits the domain through the central channel outlet (Figure 17(b)). The velocity in the inlet channels gradually reduces in the along-the-channel direction, and the opposite is observed for the velocity in the outlet channel.

Figure 18 shows a comparison of the observed pressure drop at varying flow rates for the serpentine and the interdigitated channels. It can be observed that the pressure drop obtained with the latter design is approximately six times higher

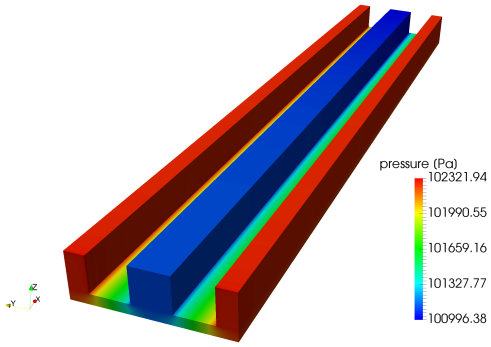

(a) Pressure distribution

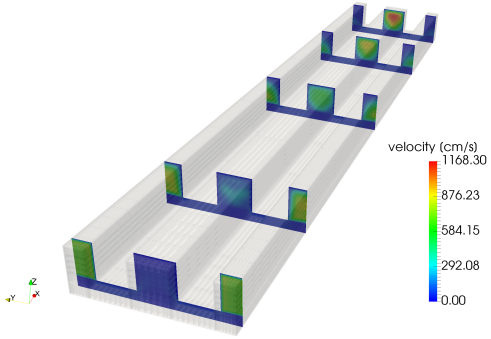

(b) Velocity profile slices along the domain

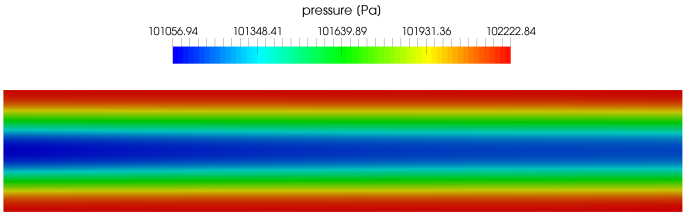

(c) Pressure profile in the plane $z = 0$

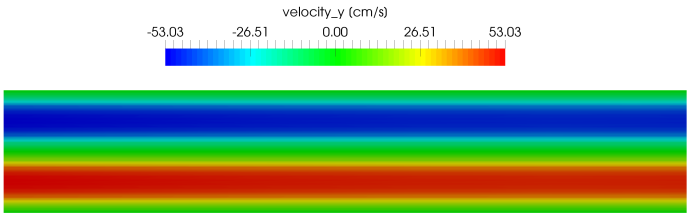

(d) Velocity profile in the plane $z = 0$

Fig. 17 (a) Pressure and (b) velocity distributions in the interdigitated channel and GDL, and (c) pressure and (d) velocity profiles in the XY-plane at $z = 0$ for the $Re = 400$ case.

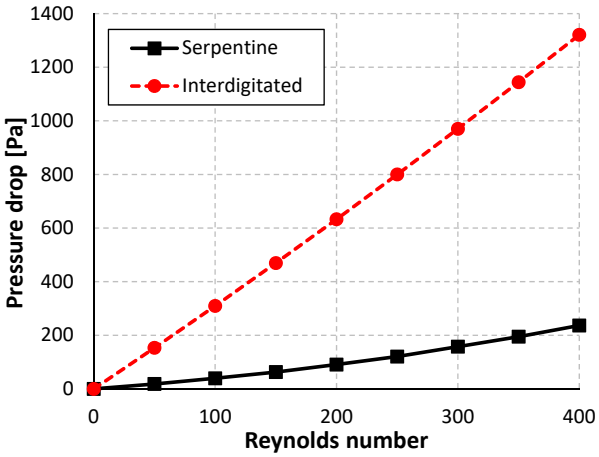

Fig. 18 Pressure drop in the serpentine and interdigitated gas channel designs at varying Reynolds numbers.

than the serpentine case, therefore, even though more gas will be available in the GDL, there is a substantial penalty in terms of pressure drop when using interdigitated designs.

In order to study compressibility effects, an incompressible solver was used to solve the mass transport problem with the interdigitated flow-field design. In this case, convergence could not be achieved thereby further justifying the use of a compressible formulation for these types of problems as already discussed in reference Santamaria et al. (2013), even though lack of convergence was not given as a justification.

6 Conclusions

A compressible, steady-state, isothermal fluid flow mathematical model is presented that is valid in both gas channel and porous media. The governing equations are obtained using the volume averaging technique. It is shown that if the phase average density and intrinsic phase average velocity are used, a continuous solution is obtained. Only this combination of averaged quantities leads to a stable, oscillation-free solution when Q_2-Q_1 Lagrange finite elements are used.

The numerical model is used to study two experimental setups developed to measure through-plane and in-plane gas permeability of fuel cell porous media. Numerical results can reproduce the experimental pressure drops reported in literature at varying flow rates in both setups. In these setups, channel-porous medium interactions are observed at high flow rates. Due to these interactions, the use of one-dimensional models to extract permeability values from experimental results can result in substantial errors, especially at high flow rates. For example, for the through-plane experimental setup under study, at flow rates of 1 SLPM a discrepancy of 12% in pressure drop was observed when using permeability values estimated with a 1D model compared to the proposed three-dimensional model. For the in-plane permeability setup, similar discrepancies are observed.

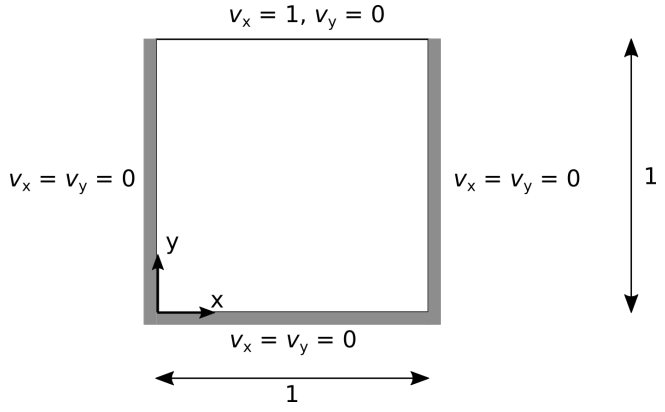

Fig. 19 Lid-driven cavity flow configuration and boundary conditions.

The suitability of the mathematical model for fuel cell applications is finally illustrated by estimating the change in pressure drop in serpentine and interdigitated flow fields in contact with a gas diffusion media.

Acknowledgements The authors would also like to thank the Natural Sciences and Engineering Research Council of Canada (NSERC), the Automotive Fuel Cell Cooperation (AFCC) Corp., and International Cooling Towers (ICT) for their financial support.

Appendix A - Lid-Driven Cavity Flow Test Case

A standard benchmark problem for testing Navier-Stokes equations is the lid-driven cavity flow problem (Donea and Huerta (2003); Cremonesi et al. (2019)), which consists in the flow of an isothermal fluid in a square cavity, as shown in Figure 19. The fluid contained inside the cavity is set into motion by the top wall which is sliding at constant velocity from left to right, while the other sides are fixed.

The steady-state compressible numerical solution is computed at $Re = 1000$ on a 128×128 grid by using Q_1 and Q_2 approximations for density and velocity, respectively. The tolerance of the Newton method is set to 10^{-10}. The fluid flow patterns generated in this computation are shown in Figures 20(a) and 20(b). The streamlines depicted in Figure 20(a) show the formation of three vortexes, which have been already observed in previous numerical studies Donea and Huerta (2003); Ghia et al. (1982); Erturk et al. (2005); Cremonesi et al. (2019).

The numerical results are compared to those previously obtained by Ghia et al. (1982). Figure 21 shows the variation of the horizontal and vertical velocity components along the vertical and horizontal centerlines (i.e., $y/L = 0.5$ and $x/L = 0.5$), respectively. The computational results obtained by the present model are in very good agreement with the available numerical data.

References

Amestoy P, Duff I, L'Excellent J (1998) MUMPS multifrontal massively parallel solver version 2.0

Auriault J (2009) On the domain of validity of Brinkmans equation. Transport in porous media 79(2):215–223

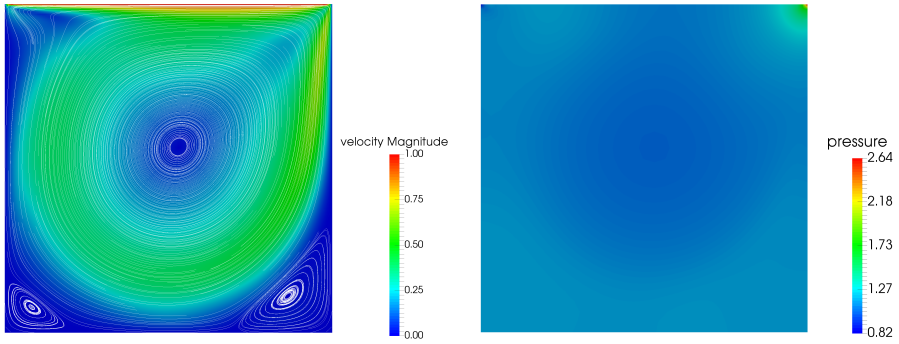

(a) Velocity distribution and streamlines (b) Pressure distribution

Fig. 20 (a) velocity field and streamlines, and (b) pressure field for the lid-driven cavity flow at Re = 1000.

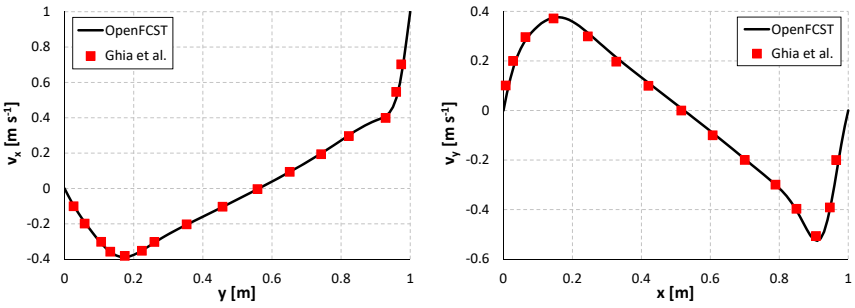

(a) Velocity $x-$component (b) Velocity $y-$component

Fig. 21 (a) velocity $x-$component profile along the vertical centerline, and (b) velocity $y-$component profile along the horizontal centerline for the lid-driven cavity flow at Re = 1000.

Badea L, Discacciati M, Quarteroni A (2010) Numerical analysis of the navier–stokes/darcy coupling. Numerische Mathematik 115(2):195–227

Bangerth W, Hartmann R, Kanschat G (2007) deal.II - a general-purpose object-oriented finite element library. ACM Transactions on Mathematical Software (TOMS) 33(4):24

Beavers G, Joseph D (1967) Boundary conditions at a naturally permeable wall. Journal of Fluid Mechanics 30(1):197–207

Bernardi C, Rebollo T, Hecht F, Mghazli Z (2008) Mortar finite element discretization of a model coupling darcy and stokes equations. ESAIM: Mathematical Modelling and Numerical Analysis 42(3):375–410

Burman E, Hansbo P (2007) A unified stabilized method for stokes' and darcy's equations. Journal of Computational and Applied Mathematics 198(1):35–51

Carrigy N, Pant L, Mitra S, Secanell M (2013) Knudsen diffusivity and permeability of PEMFC microporous coated gas diffusion layers for different polytetrafluoroethylene loadings. Journal of The Electrochemical Society 160(2):F81–F89

Chidyagwai P, Rivière B (2009) On the solution of the coupled Navier–Stokes and darcy equations. Computer Methods in Applied Mechanics and Engineering 198(47-48):3806–3820

Cremonesi M, Meduri S, Perego U (2019) Lagrangian–Eulerian enforcement of non-homogeneous boundary conditions in the Particle Finite Element Method. Computational Particle Mechanics pp 1–16

Darcy H (1857) Recherches expérimentales relatives au mouvement de l'eau dans les tuyaux, vol 1. Impr. Impériale

Davis TA (2004) Algorithm 832: Umfpack, an unsymmetric-pattern multifrontal method. ACM Transactions on Mathematical Software 30(2):196–199

Discacciati M, Quarteroni A (2009) Navier-Stokes/Darcy coupling: modeling, analysis, and numerical approximation

Dobberschütz S (2015) Effective behavior of a free fluid in contact with a flow in a curved porous medium. SIAM Journal on Applied Mathematics 75(3):953–977

Donea J, Huerta A (2003) Finite Element Methods for Flow Problems, 1st edn. John Wiley & Sons

El-Jarroudi M, Er-Riani M (2018) Homogenization of a two-phase incompressible fluid in cross-flow filtration through a porous medium. Mathematical Methods in the Applied Sciences 41(1):281–302

Erturk E, Corke T, Gökçöl C (2005) Numerical solutions of 2-D steady incompressible driven cavity flow at high Reynolds numbers. International journal for Numerical Methods in fluids 48(7):747–774

Feser J, Prasad A, Advani S (2006) Experimental characterization of in-plane permeability of gas diffusion layers. Journal of power sources 162(2):1226–1231

Forchheimer P (1901) Wasserbewegung durch boden. Zeitschrift des Vereins deutscher Ingenieure 45:1782–1788

Gebart B (1992) Permeability of unidirectional reinforcements for RTM. Journal of Composite Materials 26(8):1100–1133

Ghia U, Ghia K, Shin C (1982) High-Re solutions for incompressible flow using the Navier-Stokes equations and a multigrid method. Journal of computational physics 48(3):387–411

Gostick J, Fowler M, Pritzker M, Ioannidis M, Behra L (2006) In-plane and through-plane gas permeability of carbon fiber electrode backing layers. Journal of Power Sources 162(1):228–238

Gray W, Lee P (1977) On the theorems for local volume averaging of multiphase systems. International Journal of Multiphase Flow 3(4):333–340

Gresho P, Sani R (1998) Incompressible flow and the finite element method. Volume 1: Advection-diffusion and isothermal laminar flow. John Wiley and Sons, Inc., New York, NY (United States)

Gurau V, Bluemle M, Castro ED, Tsou Y, Jr TZ, Jr JM (2007) Characterization of transport properties in gas diffusion layers for proton exchange membrane fuel cells: 2. absolute permeability. Journal of Power Sources 165(2):793–802

Hashemi F, Rowshanzamir S, Rezakazemi M (2012) CFD simulation of PEM fuel cell performance: effect of straight and serpentine flow fields. Mathematical and Computer Modelling 55(3-4):1540–1557

Hendrick A, Erdmann R, Goodman M (2012) Practical considerations for selection of representative elementary volumes for fluid permeability in fibrous porous media. Transport in porous media 95(2):389–405

Howes F, Whitaker S (1985) The spatial averaging theorem revisited. Chemical engineering science 40(8):1387–1392

Hsu C, Cheng P (1990) Thermal dispersion in a porous medium. International Journal of Heat and Mass Transfer 33(8):1587–1597

Hussaini I, Wang C (2010) Measurement of relative permeability of fuel cell diffusion media. Journal of Power Sources 195(12):3830–3840

Ismail M, Damjanovic T, Hughes K, Ingham D, Ma L, Pourkashanian M, Rosli M (2009) Through-plane permeability for untreated and PTFE-treated gas diffusion layers in proton exchange membrane fuel cells. Journal of fuel cell science and technology 7(5):051016

Ismail M, Damjanovic T, Ingham D, Ma L, Pourkashanian M (2010) Effect of polytetrafluoroethylene-treatment and microporous layer-coating on the in-plane permeability of gas diffusion layers used in proton exchange membrane fuel cells. Journal of Power Sources 195(19):6619–6628

Ismail M, Borman D, Damjanovic T, Ingham D, Pourkashanian M (2011) On the through-plane permeability of microporous layer-coated gas diffusion layers used in proton exchange membrane fuel cells. international journal of hydrogen energy 36(16):10392–10402

Jian Q, Ma G, Qiu X (2014) Influences of gas relative humidity on the temperature of membrane in PEMFC with interdigitated flow field. Renewable energy 62:129–136
Levy T, Sanchez-Palencia E (1975) On boundary conditions for fluid flow in porous media. International Journal of Engineering Science 13(11):923–940
Li S, Sundén B (2018) Effects of gas diffusion layer deformation on the transport phenomena and performance of PEM fuel cells with interdigitated flow fields. International Journal of Hydrogen Energy 43(33):16279–16292
Liu S, Masliyah J (1996) Single fluid flow in porous media. Chemical Engineering Communications 148(1):653–732
Mahmoudi A, Ramiar A, Esmaili Q (2016) Effect of inhomogeneous compression of gas diffusion layer on the performance of PEMFC with interdigitated flow field. Energy Conversion and Management 110:78–89
Mangal P, Dumontier M, Carrigy N, Secanell M (2014) Measurements of permeability and effective in-plane gas diffusivity of gas diffusion media under compression. ECS Transactions 64(3):487–499
Mangal P, Pant L, Carrigy N, Dumontier M, Zingan V, Mitra S, Secanell M (2015) Experimental study of mass transport in pemfcs: through plane permeability and molecular diffusivity in gdls. Electrochimica Acta 167:160–171
Nguyen P, Berning T, Djilali N (2004) Computational model of a PEM fuel cell with serpentine gas flow channels. Journal of Power Sources 130(1-2):149–157
Orogbemi O, Ingham D, Ismail M, Hughes K, Ma L, Pourkashanian M (2018) Through-plane gas permeability of gas diffusion layers and microporous layer: effects of carbon loading and sintering. Journal of the Energy Institute 91(2):270–278
Pant L, Mitra S, Secanell M (2012) Absolute permeability and Knudsen diffusivity measurements in PEMFC gas diffusion layers and micro porous layers. Journal of Power Sources 206:153–160
Park J, Li X (2007) An experimental and numerical investigation on the cross flow through gas diffusion layer in a PEM fuel cell with a serpentine flow channel. Journal of Power Sources 163(2):853–863
Park J, Li X (2011) An analytical analysis on the cross flow in a PEM fuel cell with serpentine flow channel. International Journal of Energy Research 35(7):583–593
Pharoah J (2005) On the permeability of gas diffusion media used in PEM fuel cells. Journal of Power Sources 144(1):77–82
Qin Y, Liu G, Chang Y, Du Q (2018) Modeling and design of PEM fuel cell stack based on a flow network method. Applied Thermal Engineering 144:411–423
Rajagopal K (2007) On a hierarchy of approximate models for flows of incompressible fluids through porous solids. Mathematical Models and Methods in Applied Sciences 17(02):215–252
Saffman P (1971) On the boundary condition at the surface of a porous medium. Studies in applied mathematics 50(2):93–101
Saha L, Oshima N (2012) Prediction of flow crossover in the GDL of PEFC using serpentine flow channel. Journal of Mechanical Science & Technology 26(5):1315–1320
Saha S, Kurihara E, Shi W, Oshima N (2008) Numerical study of pressure drop in the separator channel and gas diffusion layer of polymer electrolyte fuel cell and deformation effect of porous media. In: ASME 2008 6th International Conference on Nanochannels, Microchannels, and Minichannels, American Society of Mechanical Engineers, pp 1317–1325
Salahuddin K, Oshima N (2013) Numerical investigation of cross flow on the performance of polymer electrolyte fuel cell. Journal of Thermal Science and Technology 8(3):586–602, DOI 10.1299/jtst.8.586
Salahuddin K, Nishimura A, Oshima N, Saha L (2013) Numerical study of pressure drop mechanism and cross flow behavior in the gas channel and porous medium of a polymer electrolyte membrane fuel cell. Journal of Thermal Science and Technology 8(1):209–224
Santamaria A, Cooper N, Becton M, Park J (2013) Effect of channel length on interdigitated flow-field PEMFC performance: A computational and experimental study. International journal of hydrogen energy 38(36):16253–16263
Secanell M, Putz A, Wardlaw P, Zingan V, Bhaiya M, Moore M, Zhou J, Balen C, Domican K (2014) OpenFCST: An Open-Source Mathematical Modelling Software for Polymer Electrolyte Fuel Cells. ECS Transactions 64(3):655–680
Srinivasan S, Rajagopal K (2014) A thermodynamic basis for the derivation of the Darcy, Forchheimer and Brinkman models for flows through porous media and their generalizations.

International Journal of Non-Linear Mechanics 58:162–166
Sun L, Oosthuizen P, McAuley K (2006) A numerical study of channel-to-channel flow cross-over through the gas diffusion layer in a PEM-fuel-cell flow system using a serpentine channel with a trapezoidal cross-sectional shape. International journal of thermal sciences 45(10):1021–1026
Tamayol A, McGregor F, Bahrami M (2012) Single phase through-plane permeability of carbon paper gas diffusion layers. Journal of Power Sources 204:94–99
Urquiza J, N'dri D, Garon A, Delfour M (2008) Coupling Stokes and Darcy equations. Applied Numerical Mathematics 58(5):525–538
Vafai K, Tien C (1981) Boundary and inertia effects on flow and heat transfer in porous media. International Journal of Heat and Mass Transfer 24(2):195–203
Whitaker S (1969) Advances in theory of fluid motion in porous media. Industrial & engineering chemistry 61(12):14–28
Whitaker S (1996) The forchheimer equation: a theoretical development. Transport in Porous media 25(1):27–61
Whitaker S (1999) The method of volume averaging, vol 13. Springer Science & Business Media
Xu H (2019) Experimental measurement of mass transport parameters of gas diffusion layer and catalyst layer in pem fuel cell. Master's thesis, University of Alberta
Yu L, Ren G, Qin M, Jiang X (2009) Transport mechanisms and performance simulations of a PEM fuel cell with interdigitated flow field. Renewable Energy 34(3):530–543
Zhang S, Reimer U, Beale S, Lehnert W, Stolten D (2019a) Modeling polymer electrolyte fuel cells: A high precision analysis. Applied energy 233:1094–1103
Zhang X, Zhang X, Taira H, Liu H (2019b) Error of Darcy's law for serpentine flow fields: Dimensional analysis. Journal of Power Sources 412:391–397